

Fading in the Flow: Suppression of cold gas growth in expanding galactic outflows

Alankar Dutta,^{1,2}★ Prateek Sharma², and Max Gronke¹

¹ *Max-Planck-Institut für Astrophysik, Karl-Schwarzschild-Straße 1, 85748 Garching bei München, Germany*

² *Department of Physics, Indian Institute of Science, Bangalore 560012, Karnataka, India*

Accepted XXX. Received YYY; in original form ZZZ

ABSTRACT

Multiwavelength observations reveal multiphase outflows that play a crucial role in redistributing gas and metals in and around galaxies. Theoretical modelling of such multiphase outflows often employs wind tunnel simulations of a spherical cold ($\sim 10^4$ K) cloud facing a uniform hot ($\sim 10^6$ K) wind. However, outflows are naturally expanding and wind conditions change downstream – a crucial aspect overlooked in most idealized simulations. To address this, we examine how an expanding wind influences the survival, morphology, and dynamics of a cloud. We perform idealized hydrodynamic simulations of radiative cloud-crushing in an expanding wind, where the steady background wind is modelled using the adiabatic Chevalier & Clegg 1985 (CC85) analytic solution. Moving downstream, we find that the clouds remain locally isobaric with the wind, leading to a steep decline in their density contrast with respect to the ambient medium, and they eventually dissipate into the wind. This also suppresses the growth of cold gas mass in comparison to a plane-parallel wind since entrained clouds move into a less radiative background. Using analytic scaling arguments, we present a physical picture of cloud evolution in a CC85 wind. Cloud expansion and local pressure equilibrium are the key regulators of cold mass growth. Unlike traditional homogeneous wind tunnel simulations, our simulations account for the differential expansion experienced by the long cometary tails of clouds moving in an outflow. Consequently, a strong head-to-tail emission gradient in the filamentary cold gas tails develop – features closer to observations. In addition, we demonstrate that the dynamics of individual clouds may substantially alter the radial properties of their host multiphase outflows.

Key words: hydrodynamics; galaxies: starburst; methods: numerical; galaxies: outflows

1 INTRODUCTION

Galactic outflows, particularly those driven by starburst activities (Heckman et al. 1990; Lehnert & Heckman 1996), are pivotal in regulating galaxy evolution by expelling gas, metals, and energy (see Veilleux et al. 2020; Thompson & Heckman 2024 for reviews on galactic winds and Sarkar 2024 for a review on Fermi/eROSITA bubbles driven perpendicular to the Milky Way disk) into the circumgalactic medium (CGM; see Tumlinson et al. 2017; Faucher-Giguère & Oh 2023 for reviews on CGM) and even the intergalactic space in the case of stronger outflows, possibly powered by AGN (Oppenheimer et al. 2020; Davies et al. 2020; Keller et al. 2020). These outflows are inherently multiphase, encompassing hot, ionized gas, warm neutral and ionized components, and cold molecular clouds (Heckman et al. 2000; Thompson et al. 2016; Roberts-Borsani 2020; Veilleux et al. 2020; Vijayan et al. 2020; Fluetsch et al. 2021). Understanding the dynamics of these cold clouds within outflows is crucial, as they not only transport mass and metals, shaping star formation rates and influencing the thermal and chemical state of the CGM and the intergalactic medium (IGM), but also alter the overall dynamics of the wind itself through momentum and energy exchange (Hopkins et al. 2012; Anglés-Alcázar et al. 2017; Kim & Ostriker 2018; McQuinn & Werk 2018; Zabl et al. 2020; Belli et al. 2024).

The interaction between cold clouds and hot winds is a fundamental process not only in galactic outflows but also in many other astrophysical contexts that influence galaxy formation and evolution (Dekel & Silk 1986; Cole et al. 1994; Erb 2008; Putman et al. 2012; Pezzulli & Fraternali 2016; Naab & Ostriker 2017). These include fountain flows (Shapiro & Field 1976; Bregman 1980; Houck & Bregman 1990; Fraternali & Binney 2008; Rubin et al. 2022; Marasco et al. 2022; Li et al. 2023) that potentially give rise to high-velocity clouds (Benjamin & Danly 1997; Putman 1999; Wakker 2001; Putman et al. 2002; Binney et al. 2009; Heitsch & Putman 2009; Richter et al. 2017; Lehner et al. 2022), and the stripping of gas from satellite/jellyfish galaxies (Roediger & Brügggen 2007; Tonnesen & Bryan 2010; Steinhäuser et al. 2016; Ramatsoku et al. 2020; Franchetto et al. 2020; Poggianti et al. 2019; Campitiello et al. 2021; Deb et al. 2022) with the subsequent formation of cold gas (Ghosh et al. 2024; Roy et al. 2024) and stars (Tonnesen & Bryan 2012; Vulcani et al. 2018; Roberts et al. 2022) in their tails. The fate of these cold clouds, i.e., whether they survive and grow or are destroyed, has significant implications for the star formation rate/history of their host galaxies, as well as for the mass and energy budget of galaxies and their surrounding media. The cold gas may also condense from the hot and diffuse CGM due to thermal instability, particularly in the presence of large density fluctuations and stratification – common in CGM-like environments (e.g., Sharma et al. 2012; McCourt et al. 2012; Voit 2018; Choudhury et al. 2019; Mohapatra et al. 2020, 2022; Wibking

★ E-mail: alankard@mpa-garching.mpg.de

et al. 2025). Most importantly, observations indicate the presence of multiphase gas for most sightlines through the CGM, indicating the ubiquity of cold and hot gas sitting next to each other in different parts of galactic atmospheres.

The importance of cold clouds interacting with the surrounding medium in shaping galaxy formation has also been recently demonstrated in cosmological simulations of galaxy formation (Nelson et al. 2020; Ramesh & Nelson 2024). Observations as well as simulations suggest that similar physics of multiphase gas mixing governs the formation of Magellanic streams surrounding the large and small Magellanic clouds (D’Onghia & Fox 2016; Fox et al. 2020; Lucchini et al. 2021; Mishra et al. 2024) as well as in the fueling galaxies with cold gas by pristine cold filaments from the IGM (Kereš et al. 2005; Dekel et al. 2009; van de Voort et al. 2012; Mandelker et al. 2016, 2020; Berlok & Pfrommer 2019; Martin et al. 2019; Aung et al. 2024), especially around the cosmic noon ($z \sim 2 - 3$). Even seemingly disparate astrophysical phenomena in terms of time and length scales involved, such as the Coronal rain in the Sun, exhibit astonishing similarities with cloud-wind interaction, multiphase gas mixing, and thermal instability occurring in galactic atmospheres (Antolin et al. 2010; Antolin 2020; Kolotkov et al. 2023; Hillier et al. 2025).

Traditionally, the interaction between cold clouds and hot winds has been studied using the cloud-crushing setup (Klein et al. 1994; Xu & Stone 1995; Schiano et al. 1995; Vietri et al. 1997; Orlando et al. 2005; Nakamura et al. 2006; Scannapieco & Brügggen 2015; Zhang et al. 2017), where a cold and dense cloud is subjected to a low density hot wind in an initially isobaric condition. There have been notable differences across the simulation setups in these works, for example, whether there is an initial shock sweeping through the cloud, the inclusion of thermal conduction and magnetic fields (Shin et al. 2008; McCourt et al. 2015; Kooij et al. 2021; Hidalgo-Pineda et al. 2024), or if there are multiple clouds (Jun et al. 1996; Poludnenko et al. 2002; Pittard et al. 2005; Alūzas et al. 2012) that have greatly improved our understanding of cloud-wind interactions.

These early ‘cloud crushing’ studies have revealed a common picture in which cold clouds undergo mixing and destruction due to a combination of various hydrodynamic instabilities, such as Kelvin-Helmholtz, Rayleigh-Taylor, and Richtmyer-Meshkov, which develop as a consequence of the relative motion and subsequent momentum transfer between the cloud and the wind. A critical timescale in this context is the cloud-crushing time t_{cc} , defined as the timescale over which a shock propagates through the cloud, leading to its compression and potential destruction. This timescale, which also approximately equals the time for the growth of the unstable modes of the Kelvin-Helmholtz instability, is given by $t_{cc} = \sqrt{\chi} R_{cl} / v_{wind}$, where χ is the factor by which the cloud is over-dense compared to the wind, R_{cl} is the cloud size, and v_{wind} is the wind velocity.

A significant breakthrough in the relevance of the cloud-crushing problem to the multiphase CGM came with the discovery of a regime in which cold clouds can grow in the wind in the presence of radiative cooling (Armillotta et al. 2016, 2017; Gronke & Oh 2018; Li et al. 2020; Sparre et al. 2020; Kanjilal et al. 2021). In order to explain the origin of high-velocity clouds (HVCs) and cold extra-planar HI gas in Milky Way-like galaxies (Oosterloo et al. 2007; Fraternali 2009), Marinacci et al. 2010, 2011 carried out two-dimensional simulations of clouds (possibly uplifted from the ISM by supernovae) falling towards the Galactic disk. These are some of the earliest cloud-crushing simulations that found growth of cold gas due to radiative cooling in the wakes of clouds moving in the CGM (see review by Fraternali 2017). More recent simulations have supported this finding and have consistently shown that clouds can grow in the

regime of rapid radiative cooling. The relative shear between the cold cloud and the hot wind gives rise to a turbulent boundary layer with a short cooling time. This can lead to the entrainment of the diffuse gas into the dense medium. Such turbulent radiative mixing layers (TRMLs) have been extensively studied in recent idealized simulations covering a wide range of astrophysical conditions (Ji et al. 2019; Fielding et al. 2020; Tan et al. 2021; Yang & Ji 2023; Abruzzo et al. 2024), providing a general consistency with the results of radiative cloud-crushing simulations. While TRMLs driven by shear lead to mass growth at early times in radiative cloud crushing, after entrainment, the relative velocity between the cloud and the wind decreases and yet the dense cloud growth rate peaks in such a state without shear (Gronke & Oh 2020). This late-time growth may be interpreted as the steady, subsonic cooling flow solution that exists in spherical and cylindrical flow geometries (no such steady inflow solution exists in Cartesian geometry; Dutta et al. 2022).

Early works by Marinacci et al. 2010, 2011, which found growth of cold clouds, assume in their analytic estimate that the cooling time in the mixed phase remains very long during mixing. Later, Gronke & Oh 2018, 2020 removed this assumption and proposed an analytic criterion required for the growth of shear-driven cold clouds – if the cooling time of the gas in the turbulent boundary layers (formed in cloud-crushing) is shorter than the cloud-crushing/shear time, the cold gas in the cloud keeps growing, and the cloud acquires mass and momentum from the wind. This cooling criterion has since been verified by simulation results and translates to an equivalent threshold on cloud size, such that any cloud larger than this threshold size can grow due to the net cooling of the mixed (warm) gas. Gronke & Oh 2018 proposed this threshold cloud radius R_{thres} as

$$R_{thres} = \frac{\sqrt{\frac{\gamma k_B T_{cl}}{\mu m_p}}}{\gamma - 1} \frac{(k_B T_{cl})^2 \mathcal{M}}{X_H^2 P \Lambda(\sqrt{\chi} T_{cl})} \chi \delta^{-1} \quad (1.1)$$

$$\approx 10 \text{ pc} \left(\frac{T_{cl}}{10^4 \text{ K}} \right)^{5/2} \left(\frac{p/k_B}{10^3 \text{ K cm}^{-3}} \right)^{-1} \left(\frac{\mathcal{M}}{1.0} \right)$$

$$\left(\frac{\Lambda(\sqrt{\chi} T_{cl})}{10^{-21.29} \text{ erg cm}^3 \text{ s}^{-1}} \right)^{-1} \left(\frac{\chi}{100} \right) \delta^{-1}.$$

Here p is the background pressure, T_{cl} is the cloud temperature, \mathcal{M} is the Mach number of the wind (with respect to the hot gas sound speed), χ is the density contrast of the cloud with the wind, $\Lambda(T)$ is the radiative cooling function,¹ X_H is the total hydrogen mass fraction, and δ is a dimensionless parameter. We run simulations to numerically determine the value of δ that sets the size of the cloud when it transitions from destruction to the growth regime (see Section 3.1).

However, real galactic outflows are more complex, often exhibiting adiabatic expansion as they move downstream due to the continuous energy and mass input from starburst regions (Chevalier & Clegg 1985). This expansion leads to spatial and temporal variations in wind properties that the cloud experiences as it moves down the wind, necessitating a more generalized approach to studying cloud-wind interactions. In this paper, we extend the traditional cloud-crushing model. Moving beyond the traditional model where the background wind was considered to be uniform (which we refer to as ‘vanilla’ cloud-crushing), we investigate the behavior of cold clouds in adiabatically expanding winds powered by continuous starbursts. Through a series of hydrodynamic simulations, we analyze

¹ The radiative cooling rate per unit volume $\mathcal{L} = -n_H^2 \Lambda(T)$, where n_H is the total hydrogen number density.

how these realistic wind environments influence the survival, acceleration, and mixing of clouds. We model the radially expanding adiabatic background wind using the steady-state analytic solution of an adiabatically expanding spherical wind proposed by [Chevalier & Clegg 1985](#) (CC85 hereafter) for starburst-driven outflows. In a CC85 wind, an injection radius exists within which continuous star formation (and subsequent supernovae) injects mass and (thermal-)energy at a constant rate, which drives a steady wind. The wind transitions from a subsonic regime to a supersonic regime as it moves past the injection radius, where the Mach number of the wind is unity. In the asymptotic limit, the CC85 profile gives the wind pressure $p_{\text{wind}} \propto d^{-2\gamma}$, density $\rho_{\text{wind}} \propto d^{-2}$, and radial velocity $v_{\text{wind}} \sim \text{constant}$, where d is the distance from the center of the wind and γ is the ratio of specific heats.

Our paper is organized as follows. We present our numerical setup and discuss some of the novel techniques developed for our study in Section 2. In Section 3, we present our simulation results and analyze the cloud properties as they evolve in a CC85 wind. We show that the growth of cold clouds is suppressed in an expanding outflow and clouds become increasingly indistinguishable from the background wind as they travel downstream. In Section 4, we compare with previous simulations, and models of cloud-wind interaction and multiphase galactic outflows. We discuss models that evolve the clouds in an expanding wind using the analytic framework of radiatively cooling turbulent boundary layers. We build a physical theory of cloud evolution based on its downstream expansion, assuming it to be locally isobaric relation with the wind, backed by our simulation results. In this context, we also highlight the limitations of the existing models and simulations of cloud-wind interaction and how model parameters dramatically affect the properties of multiphase galactic outflows. We also compare with recent JWST observations of cold clouds in outflows (in M82). Finally, we summarize and conclude in Section 5.

2 PHYSICAL SETUP & NUMERICAL SIMULATIONS

Our numerical simulations use a three-dimensional grid with spherical polar coordinates. Our grid is uniformly spaced along the radial as well as along the polar and azimuthal directions. The spherical polar geometry of the grid aligns with the spherical symmetry of the CC85 wind and reduces numerical artifacts that can otherwise perturb the steady-state CC85 wind profile used as the background. We have used a modified version of PLUTO v4.4p2 in our simulations. It is a conservative finite-volume Godunov (magneto) hydrodynamics code ([Mignone et al. 2007](#)). We also include optically thin radiative cooling of gas at solar metallicity assuming photo-collisional ionization equilibrium in the presence of a ($z = 0$) Haardt-Madau extragalactic UV background ([Haardt & Madau 2012](#)). Radiative cooling in our simulation is turned off at the floor temperature of 4×10^4 K, the initial temperature of the cloud. This mimics the drastic reduction in cooling efficiency below this temperature because of the heating by the extragalactic background radiation. Further, in order to prevent deviations from the steady adiabatically expanding background, we have turned off radiative cooling in the bulk of the wind (identified with passive tracer), and only the mixed gas is allowed to cool radiatively. Thermal instability in the bulk of the background wind in the presence of radiative cooling ([Wang 1995](#); [Thompson et al. 2016](#); [Schneider et al. 2018](#); [Nguyen et al. 2024](#)) is a related but different problem – beyond the scope of our present study. We have also not considered other physical processes like magnetic fields, thermal conduction, self-gravity, etc. Since this is the first work that investi-

gates the effect of an expanding background on cloud-crushing simulations, we restrict ourselves to the minimum set of physical effects. In this controlled simulation setup, we explore the parameter space of cloud-wind interaction in an expanding background and prepare the necessary groundwork before introducing additional physical effects in the future. An additional caveat with the choice of spherical coordinates is that the cell size increases worsening the resolution downstream. However, on comparing cold mass across simulations at different resolutions (cf. Appendix D), we find the mass estimate agrees within a factor of a few – enough for our simulations to provide a robust estimate of the different scaling arguments (presented later in the paper) and reliably capture the physics of cloud-wind interaction.

2.1 Initial & boundary conditions

Our initial condition is a stationary, dense, spherical cloud of radius R_{cl} at a temperature of $T_{\text{cl}} = 4 \times 10^4$ K in the simulation domain. The cloud is initialized to be locally isobaric with the background wind. The density of the cloud (hence its temperature) is initialized to a fixed contrast χ with the background wind. The background condition outside the cloud is determined by the steady spherically symmetric solution of a CC85 wind ([Chevalier & Clegg 1985](#)). Furthermore, we have ensured that our computational domain always excludes the region within the injection radius (sonic point) of the CC85 wind. This simplifies our numerical scheme, as the fluid equations beyond the sonic point do not require the inclusion of any mass, momentum, or energy injection sources. We were able to maintain a stable and steady background wind profile in the entire simulation domain consistent with the CC85 solution by fixing the boundary condition to any particular CC85 wind profile.

2.2 Self-similarity and parameter degeneracy

Cloud-crushing simulations are self-similar across multiple parameters which are degenerate, i.e., for different sets of parameters with identical initial and boundary conditions, and scaled evolution equations, the solution is identical when appropriately scaled (a general feature in many hydrodynamic problems; see, for example, [Barenblatt & Zel'dovich 1972](#); [Kavvas & Ercan 2016](#); [Heller 2017](#); [Vinod et al. 2024](#)). However, differences in evolution can arise as a consequence of numerical errors. Determining this degeneracy across parameters is useful both in saving computational time and also in providing a robust choice of ‘code units’. A well-known example of such a degeneracy is the similarity of an incompressible flow with the same Reynolds numbers and the same (scaled) initial and boundary conditions.

2.2.1 Equations solved

The set of degenerate and independent parameters is dependent on the simulated physics. So, we first list the equations solved in our simulations here in this subsection. Incorporating the effect of radiative cooling, the following are the hydrodynamic equations which are solved,

$$\frac{\partial \rho}{\partial t} + \nabla \cdot (\rho \mathbf{v}) = 0, \quad (2.1a)$$

$$\frac{\partial}{\partial t} (\rho \mathbf{v}) + \nabla \cdot (\rho \mathbf{v} \otimes \mathbf{v} + p \mathbf{I}) = 0, \quad (2.1b)$$

$$\frac{\partial}{\partial t} \left(\frac{1}{2} \rho v^2 + e \right) + \nabla \cdot \left[\left(\frac{1}{2} \rho v^2 + e + p \right) \mathbf{v} \right] = -n_H^2 \Lambda(T). \quad (2.1c)$$

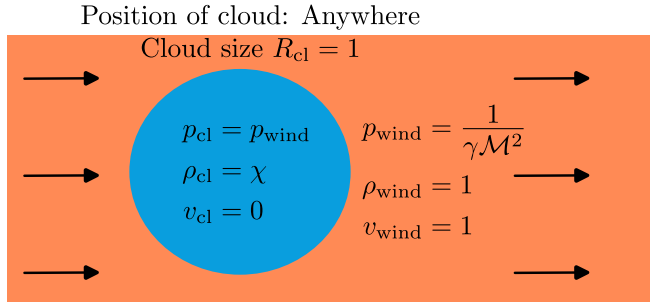


Figure 1. The initialization of a cloud crushing simulation with the choice of code units in Eqs. 2.2. This simulation setup has translational symmetry because the background wind is uniform. Therefore, the cloud can, in principle, be placed anywhere. However, we choose to place it a few cloud radii from the left edge of the simulation domain as the wind blows from left to right. This ensures that the initial bow shock and the cloud tail are reliably captured within the simulation domain.

The symbols here have their usual meaning, and this set of equations is closed by the ideal gas equation of state $e = p/(\gamma - 1)$. In the following sub-section, we show that cloud crushing simulations are degenerate in the choice of cloud density (hence the value of initial pressure).

2.2.2 De-dimensionalization of cloud-crushing in uniform wind

In this section, we outline the degenerate parameters in the cloud-crushing problem. We can de-dimensionalize Eqs. 2.1 in units of cloud size R_{cl} , cloud density ρ_{cl} , and wind velocity v_{wind} (which can be conveniently expressed in terms of the wind Mach number \mathcal{M}). Therefore, the following are the choices of units for de-dimensionalizing Eqs. 2.1,

$$L_0 = R_{\text{cl}}, \quad (2.2a)$$

$$v_0 = v_{\text{wind}} = \mathcal{M} \sqrt{\gamma \frac{k_B \chi T_{\text{cl}}}{\mu m_p}}, \quad (2.2b)$$

$$\rho_0 = \rho_{\text{wind}} = \frac{p_{\text{wind}}/k_B}{\chi T_{\text{cl}}} \mu m_p, \quad (2.2c)$$

where T_{cl} is cloud temperature, p_{wind} is the wind pressure, χ is the density contrast between the cloud and the wind (such that $\chi = \rho_{\text{cl}}/\rho_{\text{wind}}$), γ is the adiabatic index, and μ is the mean particle mass (in units of proton mass). The constants have their usual meaning. Using Eqs. 2.2, we de-dimensionalize the hydrodynamic equations into the following (using tildes to represent de-dimensionalized quantities),

$$\frac{\partial \tilde{p}}{\partial \tilde{t}} + \tilde{\nabla} \cdot (\tilde{\rho} \tilde{\mathbf{v}}) = 0, \quad (2.3a)$$

$$\frac{\partial}{\partial \tilde{t}} (\tilde{\rho} \tilde{\mathbf{v}}) + \tilde{\nabla} \cdot (\tilde{\rho} \tilde{\mathbf{v}} \otimes \tilde{\mathbf{v}} + \tilde{p} \tilde{\mathcal{I}}) = 0, \quad (2.3b)$$

$$\frac{\partial}{\partial \tilde{t}} \left(\frac{1}{2} \tilde{\rho} \tilde{v}^2 + \tilde{e} \right) + \tilde{\nabla} \cdot \left[\left(\frac{1}{2} \tilde{\rho} \tilde{v}^2 + \tilde{e} + \tilde{p} \right) \tilde{\mathbf{v}} \right] = -\zeta \tilde{n}_H^2 \tilde{\Lambda}(\tilde{T}). \quad (2.3c)$$

Here $\zeta = \frac{X_H \mu}{\gamma(\gamma-1)} \mathcal{M}^{-2} \chi^{-3/2} \left(\frac{t_{\text{cool,mix}}}{t_{\text{cc}}} \right)^{-1} \left[\frac{\Lambda(T_0)}{\Lambda(\sqrt{\chi} T_{\text{cl}})} \right]$ and $T_0 = v_0^2 \mu m_p / k_B = \mathcal{M}^2 \gamma \chi T_{\text{cl}}$, where X_H is the total hydrogen mass fraction, and μ is particle mass (in units of proton mass). With L_0 , v_0 and ρ_0 in Eqs. 2.2 as the choice of code units, the isobaric initial

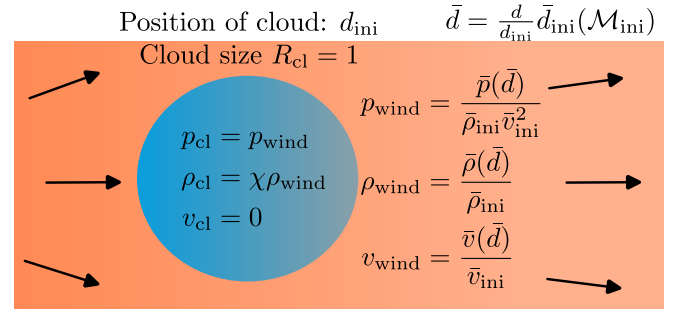


Figure 2. The initialization of a cloud crushing simulation with the choice of code units in Eqs. 2.5. Unlike ‘vanilla’ cloud crushing, here the seed cloud is embedded in a CC85 wind. This introduces a background structure to the wind and breaks the translational symmetry of the initial condition of the ‘vanilla’ cloud-crushing setup. In addition, the wind is directed radially outward instead of being plane-parallel. Refer to Section 2.2.3 for an explanation of each of the terms in this cartoon.

pressure \tilde{p} in code units is

$$\frac{p_{\text{cl}}}{\rho_0 v_0^2} = \frac{p_{\text{wind}}}{\rho_0 v_0^2} = \frac{1}{\gamma \mathcal{M}^2}, \quad (2.4)$$

where the pressures in the cloud p_{cl} and in the wind p_{wind} are initially equal because of the isobaric condition.

The initialization of cloud-crushing simulations with the choice of code units in Eqs. 2.2 is illustrated in Fig. 1. The parameters that arise in the initialization, boundary condition, and the evolution equations are the only relevant parameters in the cloud-crushing problem. The rest of the parameters, on the other hand, that do not appear in the initial or boundary conditions, as well as in the evolution equations, are degenerate. The relevant parameters are, therefore, χ , \mathcal{M} , $t_{\text{cool,mix}}/t_{\text{cc}} \propto R_{\text{thres}}/R_{\text{cl}}$, and T_{cl} .² As long as these parameters are fixed, the initial and boundary conditions, and the evolution (appropriately scaled) remain unchanged. For simulations without radiative cooling ($t_{\text{cool,mix}}/t_{\text{cc}} \rightarrow \infty$), the set of free parameters reduces to only the density contrast χ and the Mach number of the wind \mathcal{M} . It becomes degenerate for any arbitrary choice of both the initial pressure p_{wind} and the initial size of the cloud R_{cl} (see also Scannapieco & Brüggén 2015).

2.2.3 De-dimensionalization of cloud-crushing in CC85 wind

We extend this de-dimensionalization technique to simulations where clouds are seeded in expanding outflows, specifically the steadily expanding adiabatic outflows modeled by Chevalier & Clegg 1985 (CC85). The main difference between these setups and ‘vanilla’ cloud crushing is that the background wind conditions have a spatial gradient. Additionally, instead of being plane parallel, the wind is blown radially in our simulation. In this case, the most convenient choice of code units for de-dimensionalization is the wind condition at the initial position of the center of the cloud. In the de-dimensionalized form, the hydrodynamic equations remain the same as Eqs. 2.3. The

² The simulation parameters also depend implicitly on the cooling function $\Lambda(T)$ which goes in ζ defined earlier.

choice of variables for de-dimensionalization is as follows

$$L_0 = R_{\text{cl}}, \quad (2.5a)$$

$$v_0 = v_{\text{wind,ini}} = \bar{v}_{\text{ini}} \dot{M}^{-1/2} \dot{E}^{1/2}, \quad (2.5b)$$

$$\rho_0 = \rho_{\text{wind,ini}} = \bar{\rho}_{\text{ini}} \dot{M}^{3/2} \dot{E}^{-1/2} d_{\text{inj}}^{-2}. \quad (2.5c)$$

Here, \bar{v}_{ini} and $\bar{\rho}_{\text{ini}}$ are dimensionless velocity and density solutions respectively of the [CC85](#) profile at the initial position of the center of the cloud³ d_{ini} . The steady injection rates of energy and mass are \dot{E} and \dot{M} respectively within an injection region with radius d_{inj} (sometimes also called the sonic radius as the Mach number of the wind there is unity) in a [CC85](#) wind. The distance from the center of the wind in the dimensionless [CC85](#) profile \bar{d} is expressed in terms of the injection radius d_{inj} , such that $\bar{d}_{\text{ini}} = d_{\text{ini}}/d_{\text{inj}}$. In cloud-crushing simulations, the Mach number of the wind at the initial position of the center of the cloud \mathcal{M}_{ini} is a free parameter. Therefore, inverting the [CC85](#) profile using \mathcal{M}_{ini} , we get \bar{d}_{ini} , which is thus uniquely specified by \mathcal{M}_{ini} as the Mach number profile of the wind $\mathcal{M}(\bar{d})$ in [CC85](#) is an invertible function. Further, utilizing the value of \bar{d}_{ini} , we determine the dimensionless [CC85](#) wind properties $\bar{\rho}_{\text{ini}}$, \bar{v}_{ini} and \bar{p}_{ini} at the initial position of the cloud to set up the conversion between physical units and code units (see Eqs. 2.5). The distance of any arbitrary point in the simulation domain with respect to the injection radius (needed to set the [CC85](#) wind at that point) is $\bar{d} = (d/d_{\text{inj}})(d_{\text{ini}}/d_{\text{inj}}) = (d/d_{\text{ini}})\bar{d}_{\text{ini}}$, where (d/d_{ini}) is the distance of the arbitrary point with respect to the initial position of the cloud in any unit (code/physical) and \bar{d}_{ini} is actually a function $\bar{d}_{\text{ini}}(\mathcal{M}_{\text{ini}})$ obtained from \mathcal{M}_{ini} as described earlier. We use this distance \bar{d} to populate the background wind condition in the simulation domain using the [CC85](#) profile. The initial condition in the code units is illustrated in Fig. 2.

The set of independent free parameters for the cloud-crushing simulations in a [CC85](#) wind remains the same as those in ‘vanilla’ cloud-crushing, i.e., χ , \mathcal{M}_{ini} , $t_{\text{cool,mix}}/t_{\text{cc}}|_{\text{ini}}$ and T_{cl} except for an additional parameter $d_{\text{ini}}/R_{\text{cl}}$. This parameter $d_{\text{ini}}/R_{\text{cl}}$ comes from the initialization of the [CC85](#) wind using $\bar{d} = [(d/R_{\text{cl}})/(d_{\text{ini}}/R_{\text{cl}})]\bar{d}_{\text{ini}}$, where (d/R_{cl}) and $(d_{\text{ini}}/R_{\text{cl}})$ are positions of any point in the simulation domain and the initial center of the cloud in code units, respectively. This wind profile breaks the translation symmetry of ‘vanilla’ cloud crushing simulations and introduces the spatially changing background, normalized by the wind properties at the initial position of the cloud. This additional free parameter $(d_{\text{ini}}/R_{\text{cl}})$ ensures that clouds arbitrarily placed in the wind will experience different background wind conditions and evolve differently. Naturally, more degenerate quantities arise here. They are namely \dot{E} , \dot{M} , d_{inj} , and R_{cl} , which are all absorbed in the conversion factors between the physical and code units (see Eqs. 2.5). A minor caveat here is that in our simulations the initial cloud is not strictly held at a fixed density contrast χ , but has a small spread about it (depending on its size R_{cl}) in order to fix the initial cloud temperature T_{cl} to 4×10^4 K, the temperature floor in our simulations.

2.2.4 Simulation parameters

The values of the simulation parameters are listed in Table 1. The wind properties are chosen close to the values used in [Chevalier &](#)

[Clegg 1985](#), appropriate for the outflow in the M82 galaxy. The cloud properties and the initial Mach number of the wind are chosen to be similar to the previous cloud-crushing simulations like [Gronke & Oh 2018, 2020](#); [Kanjilal et al. 2021](#). This choice of free (and degenerate) parameters enables meaningful comparisons with previous studies and helps isolate the effects introduced by incorporating the expanding background of the outflow in our simulations.

2.3 Cloud identification

Previous uniform cloud-crushing simulations identify clouds as a collection of gas cells that are cold and dense. Since the cells are roughly isobaric and the background pressure is fixed in this case, a denser cell is also cooler by the same factor. This is not the case in a [CC85](#) wind where the background pressure decreases with distance. Thus, as the cloud moves downstream in the wind, it is close to the temperature floor, but its density reduces because it is isobaric relative to the falling background pressure. At some point, the density contrast relative to the background can become smaller than a chosen density contrast. We use two thresholds for cloud identification: (i) cold grid cells with temperature $< 2T_{\text{cl}} = 8 \times 10^4$ K, and (ii) cold ($< 2T_{\text{cl}}$) and overdense ($\rho > 10\rho_{\text{wind}}$) cells. Criterion (ii) excludes cold gas that is not sufficiently dense relative to the background, and thus the cold+dense cloud mass decreases at late times for all runs since a locally isobaric cloud continuously reduces its density relative to the background wind (c.f. Fig. 6).

A key caveat is that our analysis is limited to a subset of the simulation domain where the background wind temperature, based on the [CC85](#) profile, remains above 8×10^4 K. To ensure consistency, we define a sub-domain with $T_{\text{wind}} \geq 9 \times 10^4$ K for all cloud identification based on this temperature threshold. Beyond this region, the wind becomes both cold and diffuse due to adiabatic expansion, making it difficult to distinguish between cold gas originating from radiative cooling in turbulent mixing layers (triggered by cloud-crushing) and that formed via adiabatic expansion of the wind.

2.4 Cloud tracking scheme

Cloud-crushing setups generally result in an advection of the initial seed cloud along the direction of the wind. This usually causes a part of the cloud or the entirety of it to move out of the simulation domain quickly. Large simulation domains can solve this issue at the cost of computations becoming prohibitively expensive. In order to overcome this, cloud crushing simulations generally employ a continuous Galilean frame transformation, which loosely follows the center of mass of the cloud material as described in [Kanjilal et al. 2021](#); [Gronke & Oh 2018](#); [Dutta & Sharma 2019](#) and [Shin et al. 2008](#).⁴ The frame transformation procedure used in previous works changes the absolute values of the coordinate positions in the simulation domain. In Cartesian coordinates, after any frame transformation, the geometry and sizes of the grid cells, as well as the underlying fluid equations, remain unchanged, as they are independent of the absolute values of the grid positions. However, for the case of spherical coordinates (used in this work), an additional complication is that the cell size and the geometry dependent source terms in the fluid equations

³ The [CC85](#) density, pressure, and velocity profiles are de-dimensionalized using $\dot{M}^{3/2} \dot{E}^{-1/2} d_{\text{inj}}^{-2}$, $\dot{M}^{1/2} \dot{E}^{1/2} d_{\text{inj}}^{-2}$, and $\dot{M}^{-1/2} \dot{E}^{1/2}$ respectively. They are denoted by overbars. With this normalization, all the [CC85](#) profiles exactly trace each other, with distance in units of d_{inj} .

⁴ This procedure can also be simulated with equivalent source terms in the Euler equations and can, in principle, be extended with a time-dependent boundary condition to take into account a background having spatial variations as described and implemented by [Tan et al. 2023](#) in Cartesian coordinates.

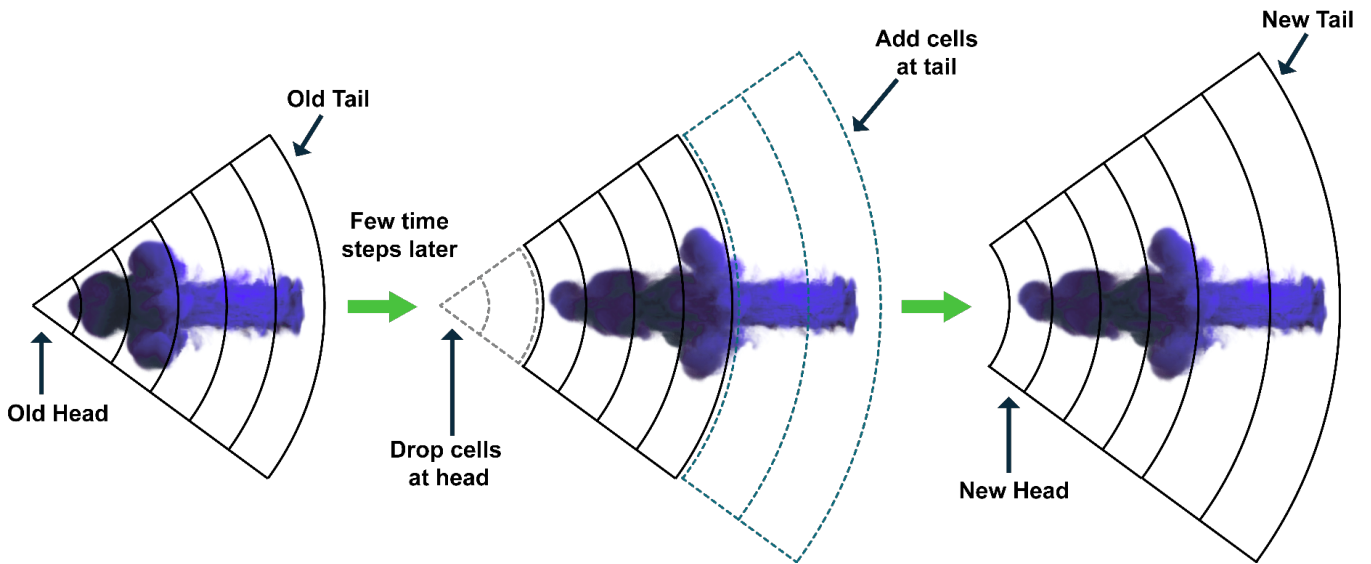


Figure 3. Illustration of our novel ‘cloud-tracking’ algorithm. This algorithm is generic and can take into account a spatially varying background profile in any coordinate system. However, particular to our work, we use spherical coordinates which matches with the natural geometry of a **CC85** wind. We track the center of mass of the cloud material, marked by a passive tracer. Whenever this moves by more than 1 cell length and the leftmost position of the tracer is more than $16 R_{c1}$ from the leftmost edge of the domain, we ‘effectively’ drop the cells from the left (*head*), introduce an identical number of cells to the right (*tail*) and fill them with the **CC85** solution at their respective position. This procedure dynamically clips the simulation domain from the left (wind entry) and extends it to the right (wind exit) ensuring that a relatively small computational domain can follow a moving cloud and prevents its tail to quickly leak out of the simulation box.

depend on the absolute values of the coordinate positions. Therefore, a Galilean frame transformation scheme cannot simply be implemented without a continuous change in the underlying grid. This brings additional complications to the numerical setup. On the other hand, the choice of spherical coordinates is particularly convenient to study outflows, as the grid aligns with the geometry of the background field and does not introduce numerical artifacts that cause deviation from the steady-state **CC85** solution that we encountered on trying to initialize a **CC85** wind in cartesian boxes.

Bearing these in mind, we have developed a new algorithm of ‘cloud tracking’ that can be applied to outflows or any other generic wind-tunnel simulations with spatially varying wind condition in any coordinate system and does not involve continuously changing the underlying grid. In the remainder of this subsection, we describe the implementation of this cloud tracking scheme. A tracer field (which passively advects with the flow) tags the ‘initial’ cloud material in our numerical setup. At each time step in our simulation, we calculate the leftmost (innermost/minimum) radial extent of the passive tracer by considering cells having tracer amounts above a threshold of 10^{-4} . Our tracking scheme tries to keep this position of the minimum radial extent of the passive tracer within a fixed distance from the leftmost (innermost) radial edge of the simulation domain. This tracking procedure, therefore, switches on or off depending on the distance between the innermost radial extent of the passive tracer and the left edge of the simulation domain, which we fix to $16 R_{c1}$.

When tracking is active, we calculate the radial distance moved by the center of mass of the tracer material. Whenever this distance exceeds a pre-set integer number of cells in the radial direction (we term this as the ‘shifting threshold’ and set it to 1), we shift the fluid profile by the same number of cells radially inward. This is achieved by eliminating cells at the innermost edge and introducing identical numbers of cells down the wind at the outermost edge of the simulation domain. These newly introduced cells at the right edge of the simulation domain are assigned the background **CC85** wind

condition according to their distance from the center of the wind. We also update the coordinate positions and cell sizes of these newly introduced cells (in spherical geometry). Therefore, our tracking algorithm effectively clips the simulation domain, on-the-fly, from the left (wind entry) and extends the domain to the right (wind exit) as the cloud gradually travels downstream. Although, in principle, this algorithm can work for any arbitrary cell size, our numerical implementation of this tracking scheme assumes uniform grid spacing both along the radial and the angular (polar and azimuthal) directions for simplicity.

This cloud tracking scheme ensures that even with relatively small sized simulation domain, most of the cloud material remains within the domain for the maximum amount of time. In addition, it takes care of the spatially changing background wind in spherical coordinates. Our cloud tracking algorithm is schematically illustrated in Fig. 3. Carried by the wind blowing from from left to right, the cloud moves to the right. In response, our scheme shifts the fluid fields to the left. It is worth noting that the number of ghost cells needed for this tracking scheme to work must be more than what is required by the reconstruction stencil, plus the ‘shifting threshold’. This ensures that the ghost cells communicated across multiple processors (for internal boundaries) contain correct values of the fluid fields required by the reconstruction stencil after any shifting by the tracking algorithm. Once the shifting is complete, one or more ghost cells at the edge will have spurious values of the fluid fields. However, as long as these cells are not utilized in the reconstruction stencil, it is safe to allow this. It is worth noting that, in contrast to the previously used cloud tracking algorithms, we never switch the frame of reference here, and the simulation is always carried out in the initial lab frame.

Table 1. Parameters of cloud-crushing simulations in CC85 wind

Set 1					Set 2				
$\dot{E} = 3 \times 10^{41} \text{ erg s}^{-1}$, $\dot{M} = 2 M_{\odot} \text{ yr}^{-1}$, $d_{\text{inj}} = 200 \text{ pc}$, $d_{\text{ini}} = 214 \text{ pc}$, $p(d_{\text{ini}})/k_B = 2.02 \times 10^6 \text{ K cm}^{-3}$					$\dot{E} = 10^{42} \text{ erg s}^{-1}$, $\dot{M} = 5 M_{\odot} \text{ yr}^{-1}$, $d_{\text{inj}} = 300 \text{ pc}$, $d_{\text{ini}} = 371 \text{ pc}$, $p(d_{\text{ini}})/k_B = 1.26 \times 10^6 \text{ K cm}^{-3}$				
χ	M_{ini}	$T_{\text{cl}} [\text{K}]$	$t_{\text{cool,mix}}/t_{\text{cc}}$	$d_{\text{ini}}/R_{\text{cl}}$	χ	M_{ini}	$T_{\text{cl}} [\text{K}]$	$t_{\text{cool,mix}}/t_{\text{cc}}$	$d_{\text{ini}}/R_{\text{cl}}$
100	1.496	4.0×10^4	0.08	28.268	100	1.996	4.0×10^4	0.1	28.656
			0.1	35.335				0.2	57.313
			0.2 [†]	70.671				0.3	85.696
			0.3	106.006				0.5	143.282
			0.5	176.677				0.8	229.252
			0.8	282.684				1.0	286.565
			1.0	353.355				1.4	401.190
			1.4	494.697				2.5	716.411
			2.5	883.387				5.0	1432.823
			8.0	2826.838				6.0	1719.387
								7.0	2005.952
								8.0	2292.516

[†] The fiducial parameters

Most of the trends discussed in our paper remain the same for the two different Mach numbers at the initial positions of the cloud in different CC85 winds (Sets 1 & 2).

3 RESULTS

3.1 Radiative cooling and threshold cloud size in a uniform wind

Using our simulations (in spherical coordinates), we carry out ‘vanilla’ cloud-crushing at different cloud sizes to numerically evaluate the dimensionless parameter δ in Eq. 1.1. The choice $T_{\text{mix}} = \sqrt{\chi} T_{\text{cl}}$ is a simple approximation (Begelman & Fabian 1990) rather than a rigorous criterion. Because of this, δ would usually depend on the detailed nature of the cooling curve and the cloud/floor temperature in a simulation. Therefore, we carry out these ‘vanilla’ cloud-crushing simulations to get an estimate of the cloud radius above which clouds grow due to strong radiative cooling in a plane-parallel wind. These simulations also serve as a set of control setups against which cloud-crushing in an expanding wind can be benchmarked. Our simulation result on ‘vanilla’ cloud-crushing which we use to numerically evaluate δ is illustrated in Fig. A1 in Appendix A. We find that $\delta \approx 6$ is where the turnover from destruction to growth regime of clouds occurs in uniform cloud crushing.

3.2 Radiative cloud-crushing in an expanding background

We select clouds that are found to be growing due to radiative cooling in a uniform wind (‘vanilla’ cloud crushing) and initialize them in an expanding CC85 wind. We fix the initial cloud position and wind properties and change the cloud size by varying $t_{\text{cool,mix}}/t_{\text{cc}}|_{\text{ini}}$ to systematically explore the growth/destruction of clouds in an expanding background. Because of this, the two independent parameters in these cloud-crushing simulations, namely $d_{\text{ini}}/R_{\text{cl}}$ and $t_{\text{cool,mix}}/t_{\text{cc}}|_{\text{ini}}$, no longer remain independent (cf. Section 2.2.3). For our analysis, we consider only the sub-domain where the background wind temperature is greater than $9 \times 10^4 \text{ K}$ and classify all gas cells in this region with temperatures less than $2T_{\text{cl}} = 8 \times 10^4 \text{ K}$ as cold cloud material (cf. Section 2.3). This sub-domain is also used in the visualization in Fig. 4, where we show the evolution of the temperature field on a slice in the $x - y$ plane passing through the center of our simulation domain (along the z -axis) using a few selected snapshots. The gradient in the background wind temperature is consistent with the adiabatic expansion of a typical CC85 wind. Similar to Gronke & Oh 2020, for cooling dominated clouds, we find that their evolution in the wind can be broadly distinguished into

two different stages – (i) initial ‘tail-formation’ stage when a large relative velocity between the cloud and the wind causes the initial spherical blob of cold gas to develop a long, sheared cometary tail in the direction of the wind followed by (ii) an ‘entrained’ stage when the cold gas grows due to a gradual inflow through radiative cooling around the cloud perhaps as a local cylindrical cooling flow (Dutta et al. 2022). The scales provided with the slices in Fig. 4 also indicate the gradual expansion that the cloud has undergone perpendicular to the radial direction as it has moved down the expanding wind. We find that the cold gas is nearly isothermal, and most cloud cells have a temperature approximately equal to the floor temperature in our simulation, i.e., $4 \times 10^4 \text{ K}$. Despite having some similarities with clouds moving in a uniform wind, an expanding wind causes the cloud properties to be qualitatively different from those in a uniform wind, which we discuss further.

Fig. 5 illustrates the evolution of the cold mass of clouds with different sizes seeded in an expanding wind, and also compares it with the evolution of cold mass for the same clouds in a uniform wind (‘vanilla’ cloud-crushing) with identical initial conditions. We find that the growth of cold clouds is suppressed in an expanding wind compared to a uniform wind. An important result from our simulations is that such a suppression of cold mass for growing clouds occurs across clouds of all sizes. The smallest clouds that are in the destruction regime due to shear-induced mixing in the uniform wind (and inefficient radiative cooling) exhibit a similar reduction of their cold mass content over time and are relatively unaffected by the expanding background. Unlike clouds moving in a uniform wind, these clouds moving in an adiabatically expanding wind fail to remain dense with contrasting features from the background as they travel down the wind (cf. Section 3.3 & 3.4). The reduction in the density of the cold cloud as it moves in the wind plays a crucial role in suppressing the growth of the cold mass in an expanding background. When the time in our simulation is normalized by the initial cloud-crushing time $t_{\text{cc,ini}}$ (which is longer for larger clouds), the largest clouds travel further downstream compared to the smaller ones within the same number of cloud-crushing times. In other words, the change in the background wind condition for every cloud radius moved by a cloud increases with cloud size R_{cl} . This results in the highest suppression in mass growth and departures from ‘vanilla’ cloud-crushing for the larger clouds (smaller $t_{\text{cool,mix}}/t_{\text{cc}}|_{\text{ini}}$) in our

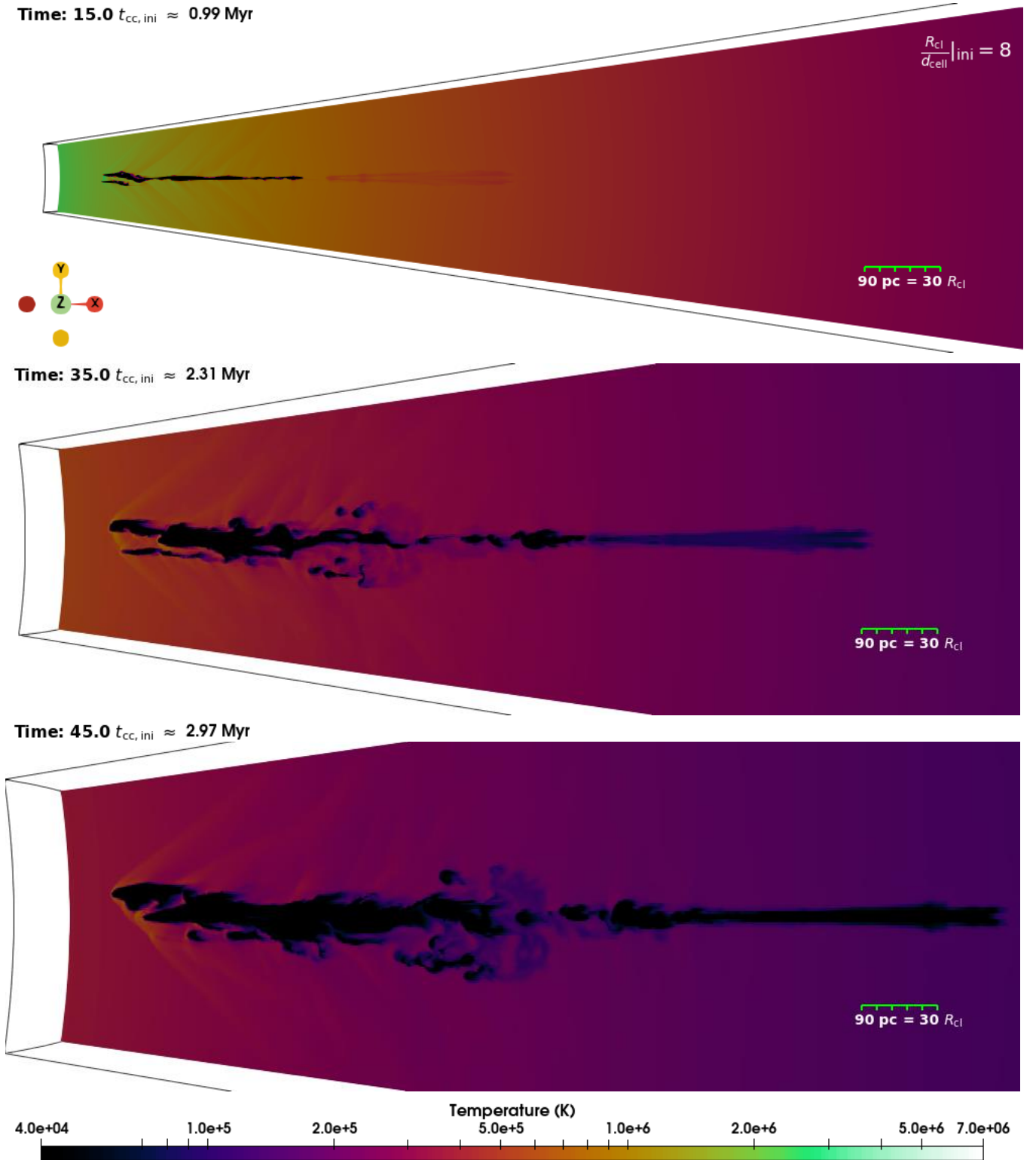


Figure 4. The temperature slices in the $z = 0$ plane from our fiducial cloud-crushing simulation in a CC85 wind. The simulation parameters are $(M, \chi, t_{\text{cool, mix}}/t_{\text{cc}}|_{\text{ini}}) = (1.496, 100, 0.2)$; cf. Table 1. We show only a few selected snapshots that clearly demonstrate the formation of elongated cold structures starting from a spherical cloud (not shown here). Similar elongated structures of cold gas with cometary tails embedded in galactic winds have been recently observed in the M82 galaxy (Bolatto et al. 2024; Fisher et al. 2025). Unlike in a uniform wind, the cloud encounters different wind conditions along its tail as it moves downstream. The cold gas also expands orthogonal to the wind direction (see the attached scale). Follow the discussion in Section 4.1.1 & Fig. 9 for a quantitative estimate on cloud expansion. Use this [link here](#) to see a video of the full evolution (also see the evolution of the corresponding density slice following [this link](#)). Moving beyond qualitative visualization, in Fig. 6, we make a detailed quantitative evaluation of the evolution of clouds in a CC85 wind.

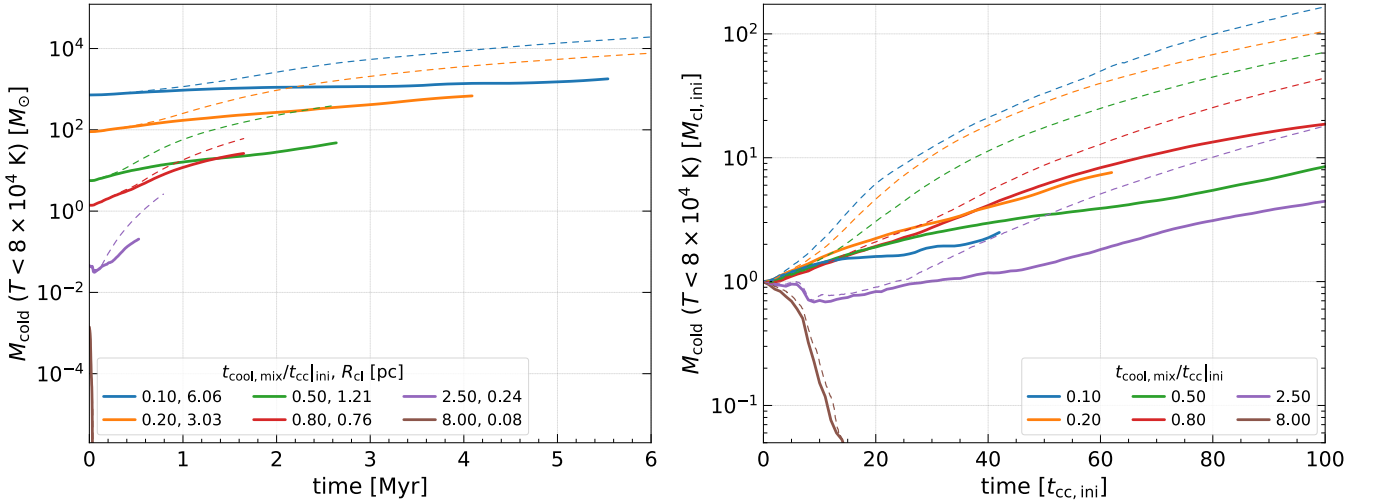


Figure 5. The temporal evolution of cold gas mass (in units of solar mass in the **left** panel and initial cloud mass in the **right** panel) in our cloud-crushing simulations for clouds of different sizes initialized in a **CC85** wind (**solid lines**) compared with identical simulations of cloud-crushing in a uniform wind (‘vanilla’ cloud-crushing in **dashed lines of the same color** as their sold counterparts). We find that the growth of cold mass is significantly suppressed in an expanding background compared to ‘vanilla’ cloud-crushing. The background wind properties and the initial position of the cloud with respect to the wind remain the same in all these simulations. In this analysis, a cell is identified as being part of the cold cloud if they have a temperature less than $2T_{\text{cl}} = 8 \times 10^4$ K. The set of constant parameters chosen for these simulations is $(M, \chi) = (1.496, 100)$ (cf. Table 1). Each line of different color corresponds to different $t_{\text{cool, mix}}/t_{\text{cc}}|_{\text{ini}} \propto R_{\text{thres}}/R_{\text{cl}}$, which translates to different cloud sizes. The time is in Myr in the **left** panel and normalized by the cloud crushing time $t_{\text{cc, ini}} = \sqrt{\chi} R_{\text{cl}}/v_{\text{wind}}$ evaluated at the initial position of the cloud (the **right** panel). The region of the simulation domain chosen for our analysis has wind temperatures greater than 9×10^4 K, higher than the temperature below which we consider gas to be cold in our analysis. For the largest clouds ($t_{\text{cool, mix}}/t_{\text{cc}}|_{\text{ini}} = 0.1, 0.2$), we truncate the evolution early after a significant portion of the initial tracer marking the cloud starts leaving our analysis domain. The largest clouds exhibit the greatest deviation in their cold mass content from their ‘vanilla’ cloud-crushing counterparts. The smallest cloud from our simulation shown in this figure ($t_{\text{cool, mix}}/t_{\text{cc}}|_{\text{ini}} = 8$) gets destroyed in both the ‘vanilla’ cloud-crushing setup and cloud-crushing in a **CC85** wind. It is relatively unaffected by an expanding wind and experiences a similar evolution in its cold mass content.

simulations. We further investigate these effects with quantitative estimates and speculate upon their implications for observations.

3.3 Properties of clouds in a typical CC85 wind

In order to explain the suppression of cold mass growth for clouds moving in an expanding wind (see Section 3.2), we investigate the properties of the cold cloud as it moves in the **CC85** wind. As usual, for our analysis, we consider only a sub-domain from our simulation where the wind temperature is greater than 9×10^4 K, and classify all the gas cells in this region at temperatures less than 8×10^4 K as cold cloud material (cf. Section 2.3).

In each snapshot from our simulation, starting from the minimum until the maximum radial extent of cold gas along the wind, we choose concentric radial shells in the wind of width $0.25 R_{\text{cl}}$. We calculate the median pressure (mass-weighted), density, and velocity of the cold gas ($T < 8 \times 10^4$ K) in each of these shells to obtain a cloud profile as a function of the downstream distance (for fiducial parameters; cf. Table 1). These pressure, density, and velocity profiles of the cloud are presented in Fig. 6, where we also show all the cloud cells as an underlying scatter plot to indicate the spread in the data. We use black dashed lines to show the corresponding **CC85** wind profile for reference. Different colors are chosen to denote cloud profiles at different times in their evolution, as labeled in the accompanying legends. From these cloud profiles, we find that the cloud pressure, in the left panel of Fig. 6, closely follows the local wind pressure (except for the small portion at the head of the cloud). Therefore, the cloud evolves roughly isobarically in the wind. Note that the median pressure is slightly lower than the local wind pressure which might be responsible for the inflow of cold gas into the cloud as

our fiducial parameter corresponds to a growing cloud with strong radiative cooling (see Section 3.5 & Fig. 8 for details). In addition, since the cold gas itself is approximately isothermal (see Fig. 4 & Section 3.5), we can approximate the cloud density as

$$n_{\text{cl}} = \frac{p_{\text{wind}}/k_B}{T_{\text{cl}}}, \quad (3.1)$$

which implies that $n_{\text{cl}} \propto p_{\text{wind}}$. Therefore, in the asymptotic limit, $n_{\text{cl}} \propto (d_{\text{cl}}/d_{\text{cl, ini}})^{-2\gamma}$, where d_{cl} and d_{ini} are the distances of the cold gas and the initial position of the cloud respectively from the wind center. Indeed the cloud density profile follows our expectation as indicated by the dotted gray curves in the middle panel of Fig. 6. The most important implication is that the cloud loses its density contrast with distance. This is generic for growing clouds of all sizes, causing them to gradually dissolve in the background wind (cf. Section 3.4). The cloud velocity profile in the rightmost panel in Fig. 6 shows that the cloud gradually catches up with the velocity of the wind. As the wind velocity in the **CC85** solution is not strictly a constant (but asymptotes to a constant), there is a substantial velocity difference between the head and the tail of the cloud, causing it to stretch in the direction of the wind.

In addition to this, we find that the inflow velocity of gas due to radiative cooling feeding the cold clouds as it moves in the **CC85** wind shows only a crude agreement with the theory of turbulent boundary layers introduced by Fielding et al. 2020; Gronke & Oh 2020; Tan et al. 2021 (see Appendix B). Further work is needed to test the limits of applicability of this theory and to come up with better models.

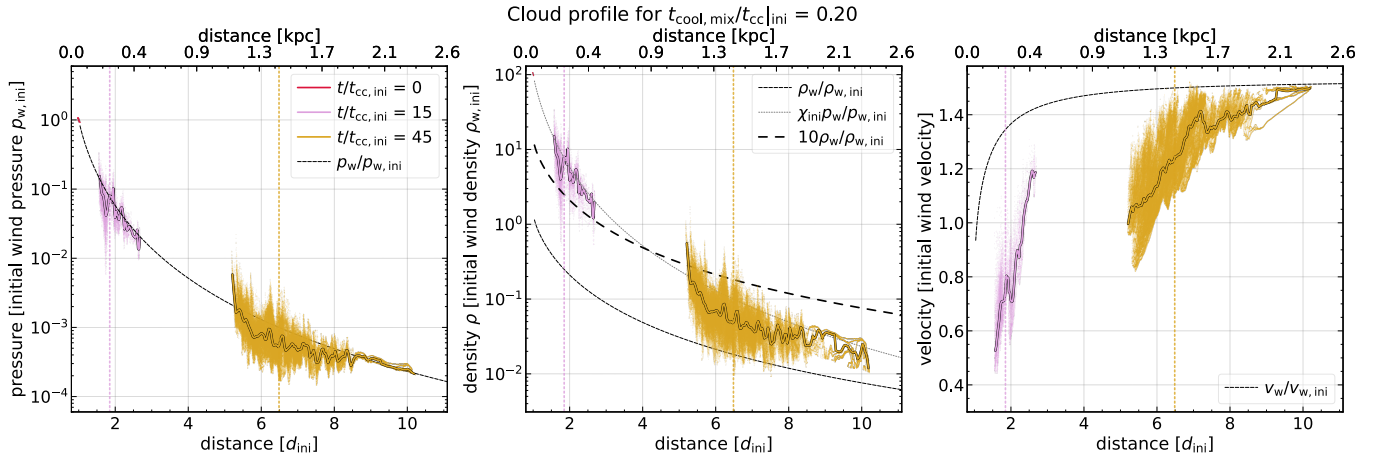


Figure 6. Temporal evolution of the profile of cloud ($T < 2T_{cl} = 8 \times 10^4$ K) pressure (**left panel**), density (**middle panel**), and velocity (**right panel**). The median cloud profiles are shown in **thin black bordered** lines, while all the cloud material is shown by dots at times 0 (**red**), 15 (**pink**), 45 (**yellow**) $t/t_{cc,ini}$. The cloud profiles are normalized by the wind properties at the initial location of the cloud. Distance down the wind is expressed in multiples of the initial position of the cloud (w.r.t. the wind center), and also in kpc (top labels). The simulation chosen for this plot corresponds to our fiducial parameters ($\mathcal{M}, \chi, t_{cool,mix}/t_{cc|ini}$) = (1.496, 100, 0.2); cf. Table 1. The **black solid** lines in all the panels show the background wind profiles, and the **vertical** lines mark the instantaneous position of the center of mass of the cold cloud (with the same color as their profile). The left panel demonstrates that the cold cloud always maintains an approximate local pressure equilibrium with the wind. This implies that the cloud density is proportional to the wind pressure ($n_{cl} \propto d_{cl}^{-2\gamma}$; cf. Eq. 3.1) at any location (because the cloud temperature is essentially fixed; cf. Fig. 8) indicated by the **thin gray dotted** line in the middle panel. The cloud median density profile approximately follows this gray line. The cloud velocity profile on the right panel shows that it gradually attains the wind velocity, with its tail becoming co-moving faster than the head. In addition, the **black dashed** line in the middle panel shows the profile of 10 times the local wind density for reference as this denotes the density cutoff used in our work to identify clouds that stand out as contrasting features with respect to their background (see Section 3.4 & Fig. 7 for details). Animated versions of this plot are available in the following links for the profiles of [pressure](#), [density](#), and [velocity](#).

3.4 Clouds as dense cold clumps embedded in a diffuse background

In the context of cloud-crushing in a **CC85** wind, the cloud encounters a cooler adiabatically expanding wind as it moves downstream. Consequently, the cold cloud formed by mixing and subsequent radiative cooling becomes diffuse as it moves further downstream. Therefore, simply identifying all the cold gas as cloud material gives an incomplete picture of the ongoing process. Considering this, we expand the definition of cloud as features formed (due to mixing and radiative cooling) as cold and dense (not just cold) relative to the featureless expanding wind. (cf. Section 2.3). In the remainder of this section we illustrate that in the presence of a **CC85** wind, the clouds in the cooling regime grow in their cold mass but at a reduced rate (see Section 3.2 & Fig. 5), and in addition continue to expand compared to clouds in a uniform plane-parallel wind. It is worth noting that the ratio of the contrast (with the background) that a cloud has between any two distances down the wind is the same for clouds of all sizes (cf. Section 3.3) if the clouds start from the same initial position with the same contrast. This ensures that the qualitative picture that clouds lose contrast while moving downstream remains unaltered by the choice of threshold density contrast (10 here; see Section 2.3).

We illustrate the evolution of the cloud mass identified using our ‘contrasting cloud identification’ criterion (discussed in Section 2.3) in Fig. 7. The different curves in the figure correspond to different initial cloud sizes in our simulation, labeled by $t_{cool,mix}/t_{cc|ini}$. The clouds in different runs from our simulation presented here are initially placed at the same position with respect to the wind (for same Mach number \mathcal{M}_{ini}) with identical conditions for the background wind. The clouds are initialized with a fixed contrast of 100 in density (or temperature) with the wind. The cloud mass evolution curves in Fig. 7 are colored according to the distance travelled by the cloud (center of mass) with respect to its initial position in the wind, as

indicated by the colorbar. As illustrated earlier in Fig. 5, although a simple identification of clouds as cold gas ($T < 8 \times 10^4$ K) in a **CC85** wind shows cloud growth (albeit at a slower rate compared to ‘vanilla’), the clouds fail to remain contrasting features in the wind. This trend holds for clouds of all sizes and occurs when the clouds reach a specific critical distance downstream. Since the cloud density at any instant only depends on its initial density and its distance from the initial position in the wind (see Eq. 3.1 in Section 3.3), the saturation of the ‘contrasting’ cold mass and subsequent turnover from growth to destruction occur at the same distance from the injection region of the wind for all clouds presented here (as they start with the same initial contrast with the background wind). Therefore, the line color in Fig. 7 (denoting the distance travelled by the cloud) at the time of the peak cold+dense mass is the same across simulation parameters (different cloud sizes). The larger clouds with smaller $t_{cool,mix}/t_{cc|ini}$ and larger $t_{cc,ini}$, travel farther downstream for every $t_{cc,ini}$ and reach the turnover distance in fewer multiples of $t_{cc,ini}$, as seen in Fig. 7 (also see the discussion near the end of Section 3.2).

3.5 Pressure-density distribution of cold gas

We analyze the distribution of the thermodynamic state of all the cold gas, with temperature less than $2T_{cl} = 8 \times 10^4$ K. This excludes the wind material that is initially cooler than this threshold, resulting in a smaller sub-domain chosen for the analysis (cf. Section 2.3). We show the distribution function at three different times from one of our cloud-crushing simulations in a **CC85** wind with $t_{cool,mix}/t_{cc|ini} = 0.2$ (the fiducial parameters; cf. Table 1) in Fig. 8. As expected, we find that the pressure and density of all gas cells are bound between the two isotherms at T_{cl} and $2T_{cl}$ indicated by dashed lines in the figure. Initially, the cloud is isobaric with the wind, but is 100 times denser. Therefore, all the cold gas initially occupies only one point in the phase space indicated by the orange diamond in Fig.

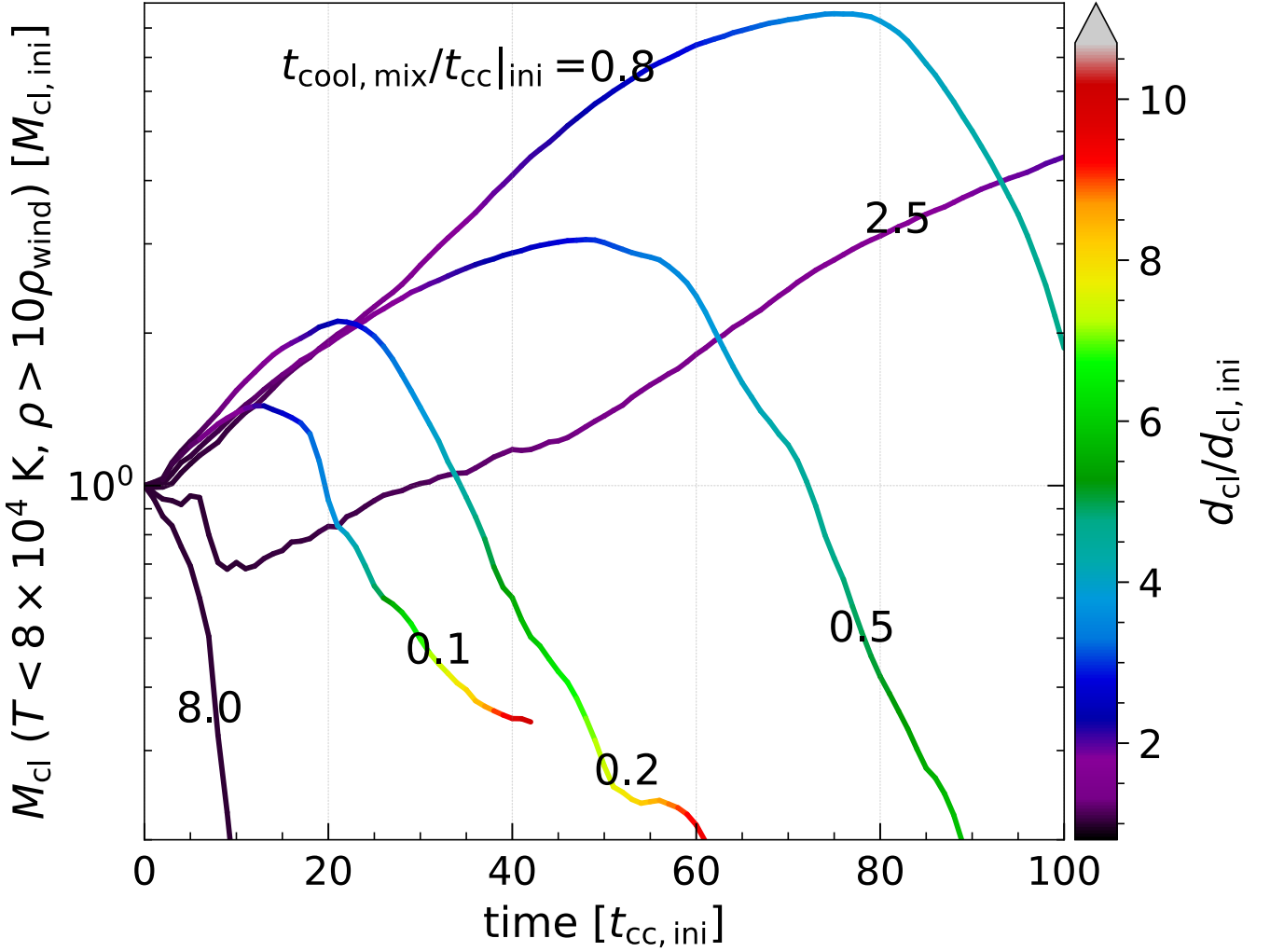


Figure 7. Temporal evolution of mass in clouds, defined as cold gas ($T < 2T_{\text{cl}} = 8 \times 10^4$ K) much denser than their local background (more than 10 times denser than the wind at their location). The gas cells satisfying this criterion stand out as contrasting radial filaments in the wind (cf. Fig. 4). The time is normalized by the initial cloud-crushing time $t_{\text{cc}, \text{ini}}$ (which is larger for larger and vice versa). Each line in the plot refers to a simulation with a fixed value of $t_{\text{cool}, \text{mix}}/t_{\text{cc}}|_{\text{ini}}$ (inversely proportional to the initial cloud size) – **annotated** by the numbers adjacent to the curves. The lines are colored according to the distance the cloud has travelled with respect to its initial position in the wind. Since the Mach number at the initial position $\mathcal{M} = 1.496$ of the cloud and its density contrast $\chi = 100$ are kept the same across all the simulations presented here, the initial cloud position $d_{\text{cl}, \text{ini}}$ is the same. The cloud density falls at a steeper rate with distance compared to the the **CC85** wind density (cf. Section 3.3). Consequently, the clouds fail to remain cold as dense contrasting features in the wind as they travel downstream. Therefore, after the cloud has travelled a critical distance down the wind (approximately the same in all simulations; cf. Eq. 3.1), the (contrasting) cloud mass transitions from an initially growing phase to a destruction phase. This transition occurs at around $d_{\text{cl}}/d_{\text{cl}, \text{ini}} \sim 4$, where the line color is blue-cyan and the grey dotted and black dashed lines intersect in the middle panel of Fig. 6.

8. With time, mixing and radiative cooling cause a spread in the properties of the cold gas, but the median density and temperature at the center of mass of the cold gas, marked by the red cross in the figure, remain very close to the T_{cl} isotherm. As expected, the red cross is a high probability region of the distribution function and can, therefore, be used as a reliable estimate of a representative thermodynamic state for the entire cloud. The inset plots in Fig. 8 show the distribution of the mass-weighted deviation of the pressure in the cold gas compared to the local wind pressure. These plots reveal that the bulk of the cold gas in the cloud attains approximate pressure equilibrium with the local background. Note that there exists a small pressure gradient between the cloud and the wind because the cloud is marginally under-pressurized. This could be either a signature of a local subsonic cooling flow that can potentially siphon cold gas into these clouds (Dutta et al. 2022), especially since such steady

solutions exist in cylindrical geometry, or partly a consequence of insufficient resolution to resolve the local cooling length (Fielding et al. 2020; also see Appendix D for a discussion on convergence in our simulations).

4 DISCUSSION

We discuss the relevance and implications of our findings in light of the existing literature in the field. We compare our simulation results and point out the discrepancies between our results and existing models/simulations. We speculate upon possible reasons and simplifying assumptions that are responsible for these differences and what they collectively imply for the multiphase cloud-wind mixing in galactic outflows. We also draw parallels from our simulations with obser-

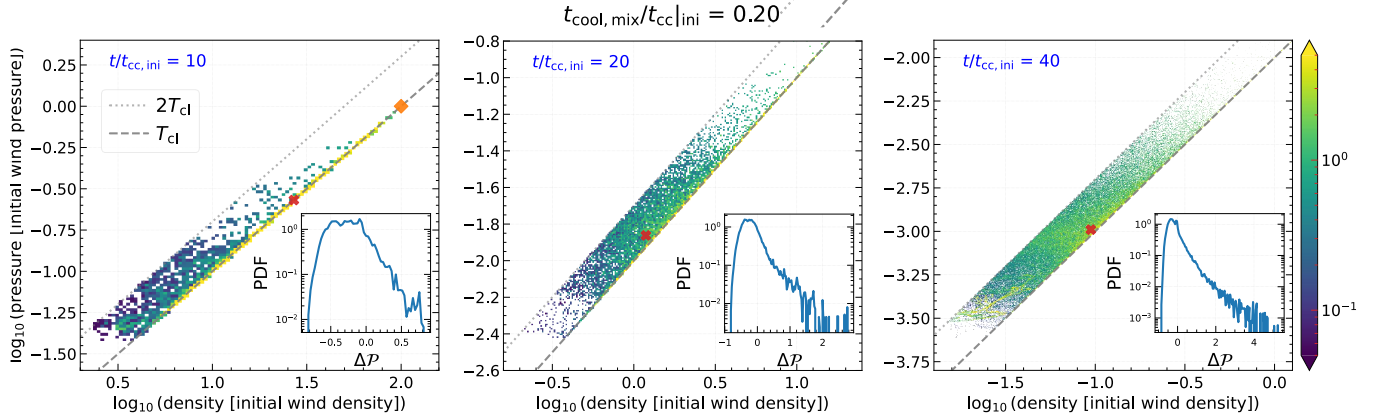


Figure 8. Temporal evolution of the phase space density-pressure distribution of the cold gas ($T < 2T_{\text{cl}} = 8 \times 10^4$ K) in our fiducial **CC85** simulation. The gas density and pressure are normalized by the wind properties at the initial location of the cloud. The different panels are at different times in the simulation as indicated by the **blue** text annotated in the plots. The **gray dashed** and **dotted** lines in all the panels show the isotherms of T_{cl} and $2T_{\text{cl}}$, respectively. The **orange** diamond in the left panel marks the position of the initial cloud material in this phase space, while the **red** cross in all the panels marks the median density and pressure of the cold gas at the instantaneous position of the center of mass of the cloud (cf. Fig. 6). With time, the cold material becomes low in density. The red cross (center of mass) always lies at the high probability region of the distribution and the distribution itself has a small spread about the $T = T_{\text{cl}}$ isotherm due to the elongated nature of the cloud as it moves downstream. Pressure fluctuations $\Delta\mathcal{P} = (p_{\text{cl}} - p_{\text{wind}})/p_{\text{wind}}$ in the cold gas compared to the local wind pressure are shown in the **inset** plot in each panel. In the inset figures, we plot the mass-weighted distribution of pressure fluctuation in the cold gas $1/M_0 (dM/d \log_{10} \Delta\mathcal{P})$, revealing that the cloud is slightly under-pressurized. An animated version of this plot is available [here](#).

vations of galactic outflows using synthetic emission maps from our simulation. At the end of this section, we discuss some of the caveats in our simulations and highlight some open questions and challenges in existing simulations and models that need further work in the future.

4.1 Comparison with previous works

There have been numerous ‘cloud-crushing’ studies (Brüggen & Scannapieco 2016; Armillotta et al. 2017; Gronke & Oh 2018; Li et al. 2020; Sparre et al. 2020; Kanjilal et al. 2021; Abruzzo et al. 2023) and a close comparison with the individual ones is beyond the scope of this section. Here, we will focus on (i) a general comparison with previous cloud-crushing studies that employ a homogeneous, non-varying background, and (ii) a closer comparison with studies that use a changing background in time and/or space similar to the one used here.

4.1.1 Homogeneous cloud-crushing simulations

While a homogeneous and non-varying background is not particularly realistic in astrophysical settings, the prior studies employing this setup focused on several different physical mechanisms at play during a cloud-wind interaction. One notable difference from simulations of cloud-crushing in a homogeneous background is that, due to the expansion of the domain, the thickness of the tail increases as the cloud moves downstream (the distance of its center of mass d_{cl} increases). In a **CC85** wind, we note that once the cloud is co-moving with the background wind, the orthogonal spread of the cloud $R_{\text{cl},\perp}$ increases with distance $\propto d_{\text{cl}}$. This is illustrated in Fig. 9 which shows the lateral extent of the clouds, calculated as the difference between the 95 and 5 percentiles of the perpendicular distance (with respect to the wind direction) of all the cold gas ($T < 8 \times 10^4$ K; cf. Section 2.3), as a function of the position of the center of mass of the cloud. In contrast, $R_{\text{cl},\perp}$ is a constant in a uniform wind. The

relation between the transverse cloud spread and the distance it travels introduces significant differences in the rate at which mass grows in entrained clouds compared to clouds in a uniform wind. We discuss using scaling relations from previous simulations of radiative turbulent mixing layers, how the orthogonal expansion of clouds can explain the suppression of cold mass growth in a **CC85** wind compared to ‘vanilla’ cloud-crushing (cf. Section 3.2 & Fig. 5).

In the entrained state (i.e., after substantial mass and momentum exchange between the cold cloud and the background wind), the rate of mass growth of a cloud $\dot{m}_{\text{cl}} \sim A_{\text{cl}} \rho_{\text{wind}} v_{\text{mix}}$ depends on the inflow velocity into the radiative mixing layers v_{mix} , the surface area of the cloud A_{cl} , and the density of the wind ρ_{wind} . We first discuss the analytic scaling relations of cloud properties and turbulent boundary layers presented in Gronke & Oh 2020 (GO20 hereafter) in light of our simulation results and then compare our findings with the simulations carried out by GO20 approximating an expanding outflow. GO20 found that the inflow velocity in the mixing layer follows $v_{\text{mix}} \sim c_{\text{s,cl}} (t_{\text{sc,cl}}/t_{\text{cool,cl}})^{1/4}$, roughly consistent with later mixing layer simulations (Fielding et al. 2020; Tan et al. 2021). GO20 assumed that the sound crossing time across the shortest dimension of the cloud remains constant. However, in a **CC85** wind, we expect the cloud lateral extent to increase with distance ($R_{\text{cl},\perp} \propto d_{\text{cl}}$; cf. Fig. 9), implying $t_{\text{sc,cl}} \sim R_{\text{cl},\perp}/c_{\text{s,cl}} \sim d_{\text{cl}}/c_{\text{s,cl}}$. Once the cloud is entrained, similar to GO20, we find that its surface area $A_{\text{cl}} \propto V_{\text{cl}}^{2/3} \sim (m_{\text{cl}}/\rho_{\text{cl}})^{2/3} \sim m_{\text{cl}}^{2/3} d_{\text{cl}}^{4\gamma/3}$ (V_{cl} is the cloud volume; see upper panel of Fig. B1 in Appendix B) due to the pressure drop $p_{\text{cl}} \propto d_{\text{cl}}^{-2\gamma}$ in a **CC85** wind.

Hence, the mass of a cold cloud in the entrained state $m_{\text{cl}} \propto d_{\text{cl}}^{5\gamma/2-9/4} \sim d_{\text{cl}}^{23/12} \approx d_{\text{cl}}^2$ (here $\gamma = 5/3$). This is a significantly steeper relation with cloud distance than what is expected from GO20 that uses a constant sound crossing time – $m_{\text{cl}} \propto d_{\text{cl}}^{5\gamma/2-3} \sim d_{\text{cl}}^{7/6} \approx d_{\text{cl}}$. In Fig. 10, we demonstrate that with the inclusion of cloud expansion in the sound crossing time, we are able to explain the steeper scaling (compared to the analytic arguments in GO20) of

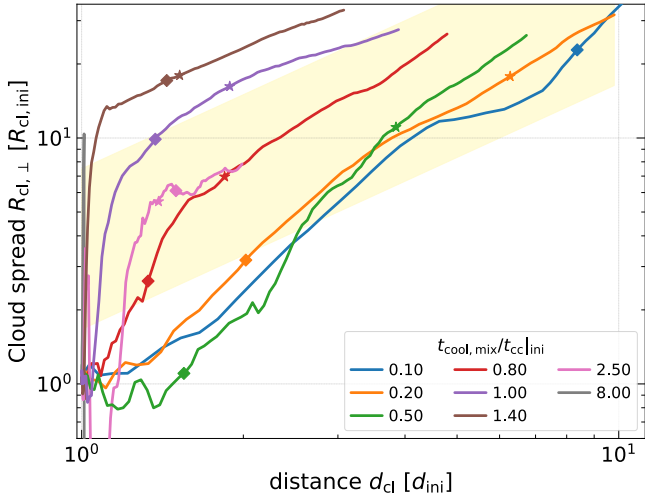


Figure 9. Evolution of the lateral extent of a cloud (in units of the initial cloud radius) as a function of the distance travelled by the center of mass of the cloud (normalized by the initial cloud distance from the center of the CC85 wind). The cloud increases in its lateral extent as it moves downstream. Along each of the curves, the diamonds denote the instant when the clouds attain twice their initial mass and the stars mark the instant when the center of mass of the clouds are travelling at 80 percent of the local wind speed – the clouds have entered an ‘entrained’ stage. Once the clouds are entrained, we expect the geometry of the CC85 wind to make the clouds spread proportional to the distance they travel, as indicated by the **yellow** band. Most of the clouds in their entrained state seem to follow this trend ($\propto d_{cl}$), except for the largest clouds (small $t_{cool, mx}/t_{cc|ini}$) which are not entrained in a significant part of their journey as well as their lateral expansion is smaller compared to their initial size.

cold mass with distance travelled by clouds that are entrained for a long time.⁵

A key distinction of clouds in a CC85 wind from homogeneous cloud-crushing studies lies in the spatial gradients of background wind properties that the cloud experiences – both along its downstream trajectory and across its internal extent from head to tail. The latter leads to interesting and potentially observable emission gradients along the cloud body (discussed further in Section 4.2), while the former may significantly influence the net cold mass growth. As demonstrated by GO20, although the background density drops with distance as $\propto d_{cl}^{-2}$, this decline is remarkably offset by the concurrent increase in the cold gas surface area and cooling time ($t_{cool, cl} \propto d_{cl}^{10/3}$) due to changing pressure conditions. However, our analytic treatment – supported by simulation results – shows that the orthogonal expansion of the cloud causes the cold mass to scale as $m_{cl} \propto d_{cl}^2$, rather than the $\propto d_{cl}$ scaling proposed by GO20. In the uniform wind scenario, both v_{mix} and ρ_{wind} are constant, resulting in an even steeper scaling of cloud mass with distance, $m_{cl} \propto d_{cl}^3$, compared to the shallower relation in an expanding wind.

Moving beyond analytic scaling estimates, we now directly compare simulation results from GO20 with ours. Specifically, GO20 studied the evolution of cold clouds in expanding outflows by employing a model of an expanding box in their simulations that approximates the azimuthal and polar expansion that the clouds undergo as they move downstream due to the geometry of the wind (also, see,

⁵ This inclusion of cloud expansion, however, weakly alters the scaling of cloud surface area with the distance travelled as the cloud traverses downstream (see Appendix B; lower panel of Fig. B1).

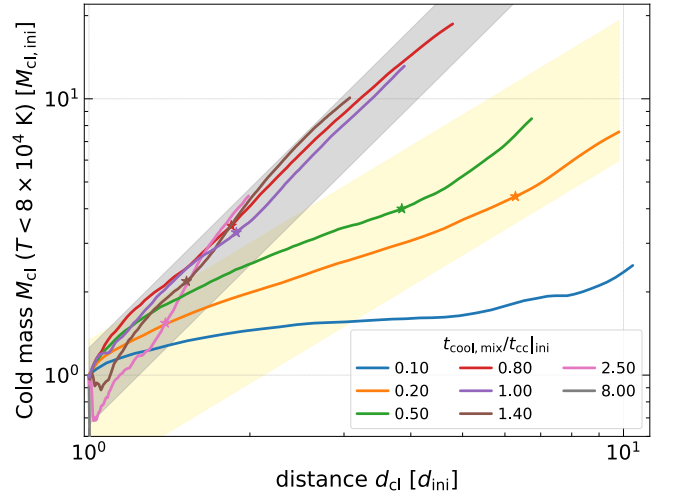


Figure 10. Evolution of the cloud mass (in units of the initial cloud mass) as a function of the distance travelled by the center of mass of the cloud (normalized by the initial cloud distance from the center of the CC85 wind). As discussed in Section 4.1.1, the increase in the lateral spread of the cloud (cf. Fig. 9) results in a steeper increase in its mass m_{cl} with distance d_{cl} ($m_{cl} \propto d_{cl}^{23/12} \approx d_{cl}^2$; **gray** band) compared to the previous estimate by Gronke & Oh 2020 ($m_{cl} \propto d_{cl}^{7/6} \approx d_{cl}$; **yellow** band; GO20). Along each of the curves, the diamonds and stars have the same meaning as in Fig. 9. The clouds which have travelled a long distance after entrainment approximately follows $m_{cl} \propto d_{cl}^2$, in line with our analytic estimates (gray band). For the largest clouds, the lateral expansion is lower compared to their initial size (closer to the $t_{sc, cl} \sim \text{const}$ assumption of GO20; yellow band). This also leads to a different scaling relation between the cloud surface area and distance travelled by the cloud compared to GO20 (cf. Fig. B1).

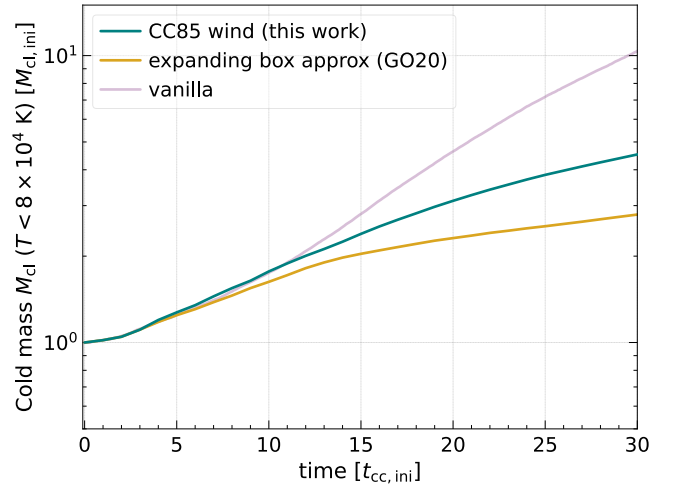


Figure 11. Comparison of the cold mass evolution of gas from our cloud-crushing simulation in CC85 wind with the cloud-crushing simulation employing an approximate expanding box model from Gronke & Oh 2020 (GO20; see Section 4.1.1 & Appendix C for details). For this comparison, we re-implemented the expanding box model used by GO20 in PLUTO and re-simulated the cloud-crushing problem using our fiducial parameters, i.e., $t_{cool, mix}/t_{cc|ini} = 0.2$ and an initial Mach number $\mathcal{M} = 1.496$ in the wind (cf. Table 1). In both the simulations, the cloud radius is initially resolved by 16 grid cells. Follow [this link](#) to see the evolution of this cloud in the expanding box simulation.

similar setups by Heitsch & Putman 2009; Tan et al. 2023 for infalling clouds). This model employs an anisotropic expansion in the simulation domain to model the CC85 wind which expands in the polar and azimuthal directions but not in the radial direction (cf. Dutta & Sharma 2019; also Scannapieco 2017 who erroneously assumed the wind to be isotropically expanding). This model assumes that the size of the cloud (and the simulation domain containing and following it) is always small enough compared to the length scale on which the wind property changes, and the wind can be assumed to be plane parallel. Therefore, under these assumptions, the entire cloud always experiences a uniform expansion perpendicular to the wind due to its movement downstream. Consequently, a local simulation domain that follows the cloud gets expanded in all directions perpendicular to the direction of the wind, determined by an expansion factor that depends on the instantaneous position of the cloud with respect to its initial position.

In contrast, our cloud-crushing simulations in an expanding CC85 wind do not make such simplifying assumptions and can account for the differential expansion of a cloud along its tail. This differential expansion of a cloud along the wind and the curvature of the wind (i.e., variation in wind properties along the cloud) become increasingly important for large clouds deeper in the cooling regime. We find that this differential expansion can lead to a lower expansion in the cloud head compared to its tail (cf. Fig. C1 in Appendix C), which, in turn, can result in an overall increase in the tail length of the cometary cloud structures (after several t_{cc}) compared to the uniform expansion considered by GO20. Moreover, the background wind properties – such as density, temperature, and pressure – vary significantly with the distance d_{cl} travelled by the cloud. Consequently, even modest discrepancies in estimating how this distance changes with time (arising from differences in how mixing/cooling between the cold cloud and hot wind progresses, which affects mass and momentum exchange) can lead to substantial differences in the predicted cold mass evolution, especially at late times.

Another difference from GO20 is that we initialize our clouds at a distance where the wind Mach number is between 1-2, not too far from the sonic point. Therefore the wind is not in the asymptotic scaling ($\rho \propto d^{-2}$, $p \propto d^{-2\gamma}$) regime, an assumption made in GO20. All of these factors potentially contribute to differences in the cold mass growth between the two simulation setups, which increase as the simulations progress further in time. This is illustrated in Fig. 11, where we compare the evolution of the cold mass in the two simulation setups for our fiducial parameters ($t_{cool,mix}/t_{cc}|_{ini} = 0.2$, and $M = 1.496$; cf. Table 1; see Appendix C for our implementation of GO20 setup). Since the cold mass estimate is slightly lower in the anisotropic expanding box of GO20 compared to our simulation domain, it might explain why GO20 reported a flatter mass-distance relation ($m_{cl} \propto d_{cl}$). We expect the differences in the cold mass estimate between these two types of simulation setups to increase further in time.

4.1.2 Semi-analytic multiphase wind models

Fielding & Bryan 2022 (FB22 hereafter) introduced a model that describes the evolution of a cold cloud that starts with some initial velocity (or from rest) in an outflow (Section 3 in their paper). FB22 assumed a steady injection of many of such clouds, possibly lifted from the ISM, at a constant rate within a region close to the center of the wind. FB22 introduced a model for the evolution of an individual cloud in a wind and used it as a source of energy, mass, and momentum injection/removal in a steady wind, assuming that clouds are introduced at a fixed rate within a central region in an outflow.

Consequently, a model to account for the evolution of a collection of small clouds continuously injected into an outflow has been utilized in developing a general framework to predict the structure of a supernovae-driven multiphase galactic outflow. Although in FB22 the single-cloud model was utilized to take into account the evolution of a collection of clouds in a spatially changing background wind (that act as source terms in the wind equation), the detailed evolution of an individual cloud in a non-uniform wind, and its comparison with simulations remain largely unexplored.⁶ The evolution of a cloud seeded in a uniform background from the single-cloud model has been illustrated in FB22. Since our work focuses on simulations of how individual clouds evolve in both a uniform and an expanding CC85 (Chevalier & Clegg 1985) wind, we are able to compare the FB22 model prediction of cloud-wind interaction with our simulation results. Furthermore, the constraints obtained by the validation of the single-cloud model would enable the construction of realistic wind profiles by providing accurate source terms in the wind equation. Prior to a comparison with FB22, it is worth noting that our work focuses on the detailed behavior of a cloud, considering a neighborhood close to the cloud. The back reaction of the cloud on the volume-filling gas that comprises the wind is beyond the scope of this work. In addition, we are mostly interested in modeling the evolution of an individual cloud and do not consider the collective impact of multiple clouds that can potentially alter the large-scale properties of the wind.

To facilitate a comparison with the cloud evolution model and the results from our simulations, we consider the single-cloud model introduced by FB22 (Section 3 in their paper).⁷ On comparing the original FB22 cloud-wind model with our simulation results, we find an unsatisfactory model prediction for the evolution of cold mass growth in a CC85 wind (see the discussion on Fig. 12 later in this section for details). Therefore, we modify the model presented by FB22 to better reproduce the evolution of the cold mass from our simulations. Next, we briefly discuss the single-cloud model by FB22. It is an empirical model of the evolution of a cloud in embedded in a hot wind. We also discuss the modifications we introduce to the parameters of the original model in order to obtain a significantly improved match with our simulation results. In the remainder of this section (and Appendix E), we describe the single-cloud model, our modifications to it, and also demonstrate how well this model compares against our simulation.

The single-cloud model introduced by FB22 is a set of coupled ordinary differential equations which can be numerically solved with some initial condition (described elaborately in Appendix E). The most important part in this model is incorporating radiative cooling of the turbulent mixing layers as the cloud moves and mixes in the wind. This essentially captures the growth/destruction of cold clouds in the wind, and it is taken into account by the factors ξ and α in Eq. E1. The key term in the model determining the cold mass evolution in the wind, is the factor α that appears as an exponent on ξ . In physical terms, α depends on the fractal dimension of the radiatively cooling turbulent mixing layer formed between the cloud and the wind due to shear-driven hydrodynamic instabilities (Mandelbrot 1975; Federrath et al. 2009; Fielding et al. 2020; Tan & Fielding 2024). Since the factor α appears in the exponent of ξ , the rate at

⁶ Albeit see the similar work by Nikolis & Gronke 2024 that carried out a direct comparison to hydrodynamical simulations.

⁷ However, for simplicity and also to compare with our simulations, we do not consider different metallicities for the cloud and the wind.

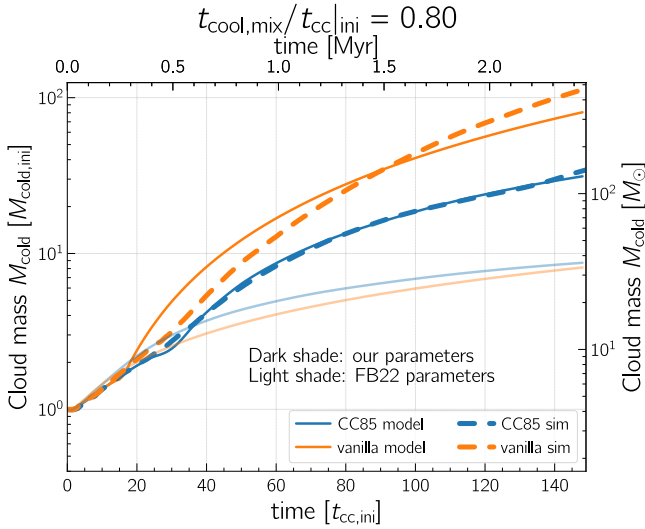


Figure 12. Comparison of the mass evolution of gas from our cloud-crushing simulation with that predicted from the FB22 single-cloud model for ‘vanilla’ cloud-crushing (in uniform wind) and for cloud-crushing in a CC85 wind (see Section 4.1.2 for details). The **dashed** lines are the simulation results for ‘vanilla’ cloud-crushing (in orange) and cloud-crushing in a CC85 background (in blue). As a specific example which would clearly demonstrate departure from model prediction, we choose the simulation result with $t_{\text{cool,mix}}/t_{\text{cc,ini}} = 0.8$ and $M = 1.496$ (cf. Table 1; not the fiducial parameter set). The corresponding model predictions are shown with **solid** lines in the same color as their dashed counterparts. The **solid light** colored lines use the original prescription from FB22 and does not match well with the simulation results. With the tuned parameters (described in Section 4.1.2 & Appendix E), we are able to achieve a better match with the simulation results – the **solid dark** colored lines. For simplicity, the free parameters of the model are chosen by visual inspection and are listed as follows, $(f_{\text{cool}}, f_{\text{mix}}, f_{\text{turb}}, C_{\text{drag}}, \xi_{\text{trans}}) = (2.0, 2.1, 0.08, 0.5, 13)$. Additionally, $f_{\text{dim}}(\xi < \xi_{\text{trans}}) = 0.49$ and $f_{\text{dim}}(\xi \geq \xi_{\text{trans}})$ equals 0.70 for vanilla cloud-crushing and 0.68 for cloud-crushing in CC85 wind. In this context, we simply demonstrate the need to construct a robust single-cloud model – a necessary step to explain the evolution of clouds in realistic outflows (cf. Fig. 13).

which cold gas forms in the FB22 model can change by orders of magnitude due to even minute changes in α .

In addition to this, simulations (Ji et al. 2019; Tan et al. 2021) show that there is a transition in the mass growth rate due to radiative cooling from the slow cooling regime (small values of ξ) to the fast cooling regime (large values of ξ) at ξ_{trans} (a free parameter in the model). According to the model introduced by Fielding et al. 2020; Fielding & Bryan 2022, this transition corresponds to a change in the fractal dimension factor f_{dim} causing a change in the value of $\alpha = (3f_{\text{dim}} - 1)/2$. Here f_{dim} follows the usual definition of fractal dimension, such that the area of a fractal surface A_{Δ} depends on the measurement scale Δ , and $A_{\Delta}/L^2 = (L/\Delta)^{f_{\text{dim}}}$, where L is the linear size of the fractal surface (Sreenivasan et al. 1989). Specifically, FB22 use $\alpha = 0.25$ for the strong cooling ($\xi > 1$) and $\alpha = 0.5$ for the weak cooling ($\xi < 1$) regime (see Section 4.3 in Tan et al. 2021 for a detailed discussion on the choice of these values).

Fig. 12 shows a comparison of our numerical simulations – both in an expanding CC85 (blue lines) as well as uniform plane-parallel wind (orange lines) – with the prediction of single-cloud evolution from the FB22 model (shown in solid light color in Fig. 12). One can see that the numerical results do not match the semi-empirical model sufficiently, with $\gtrsim 1$ dex more cold gas mass in the simulations

compared to the model. The FB22 model is also unable to reproduce the suppression of cold mass growth of clouds in an expanding wind when compared to a uniform plane-parallel wind – a definitive trend in our simulation. This is concerning, since the FB22 is used as a basis for multiphase subgrid model of galactic winds (Smith et al. 2024a,b) with the aim of being eventually incorporated into cosmological simulations. This mismatch in the cold gas mass also propagates to the overall wind properties – as we discuss below.

We also show in Fig. 12, using solid dark colored curves, a new model prediction with tuned FB22 parameters in order to reproduce the simulation data. Specifically, we changed the transition from strong to weak cooling from $\xi_{\text{trans}} = 1$ to $\xi_{\text{trans}} = 13$, and more importantly, we adjusted α to 0.235 for $\xi < \xi_{\text{trans}}$ and to 0.55 [0.52] for $\xi > \xi_{\text{trans}}$ in the uniform [expanding] wind. Crucially, this implies that mass growth, which depends very sensitively on α , is drastically different across different wind properties. Note, that while we managed to reproduce the simulation runs shown in Fig. 12 using these values,⁸ they are not robust across wind or cloud properties and would need to be adjusted depending on the wind+cloud parameters. We find that such a modification is necessary to explain the trend in the evolution of the cold mass from our simulations, especially to explain the suppression of cold mass growth in a CC85 wind compared to a uniform one. It should be noted that the FB22 model considers all gas at exactly the cloud temperature T_{cl} to be cold, whereas in our simulations, all gas cells with temperature lower than $2T_{\text{cl}}$ are considered cold. This allows us to avoid testing equality of floating-point numbers. Nevertheless, because the cloud temperature has a very tight spread about T_{cl} (cf. Section 3.5), our cold phase identification scheme to compare with FB22 model prediction is relatively robust. It is important to emphasize that we do not claim the parameters or modifications to the FB22 model presented here to be a best-fit solution. A detailed exploration of the model’s parameter space is beyond the scope of this work and is left for future studies. Our primary goal is to emphasize the need for improving existing models by calibrating them against cloud-crushing simulations in evolving background wind conditions.

FB22 also developed a framework for evolving a population of cool clouds moving in a hot wind. In this framework, the single-cloud model (described in the earlier part of this section) serves as the basis for modeling the source (or sink) terms that determine the radial profile of the wind (see the equations illustrated in Fig. 3 & Eq. 17 from FB22). These source/sink terms directly affect the energy and mass loading of the outflows. Therefore, the way individual clouds interact with the background wind determines the multiphase nature of the wind they are moving in. The FB22 prescription assumes a collection of cold clouds are continuously injected in the outflow. These clouds introduce energy and mass in both the cold and hot phases of the wind, depending on how they cool, mix and evaporate. To this end, we demonstrate that changes in the single-cloud evolution model can directly change the properties of the wind by solving the wind equation from FB22 (Fig. 3 & Eq. 17 in their paper) with different models of the single-cloud evolution. This is illustrated in Fig. 13, where we choose the same parameters for the single-cloud model as reported by FB22 (see Fig. 6 in their paper), shown in orange, to obtain a multiphase wind and compare it with the

⁸ Note that although the α values that can reproduce the evolution shown in Fig. 12 corresponds to a fractal dimension of 0.49 in the weak cooling regime and 0.7[0.68] in the strong cooling regime in a uniform [expanding] wind. These values lack sound physical justification, pointing potentially to inadequacies of the model.

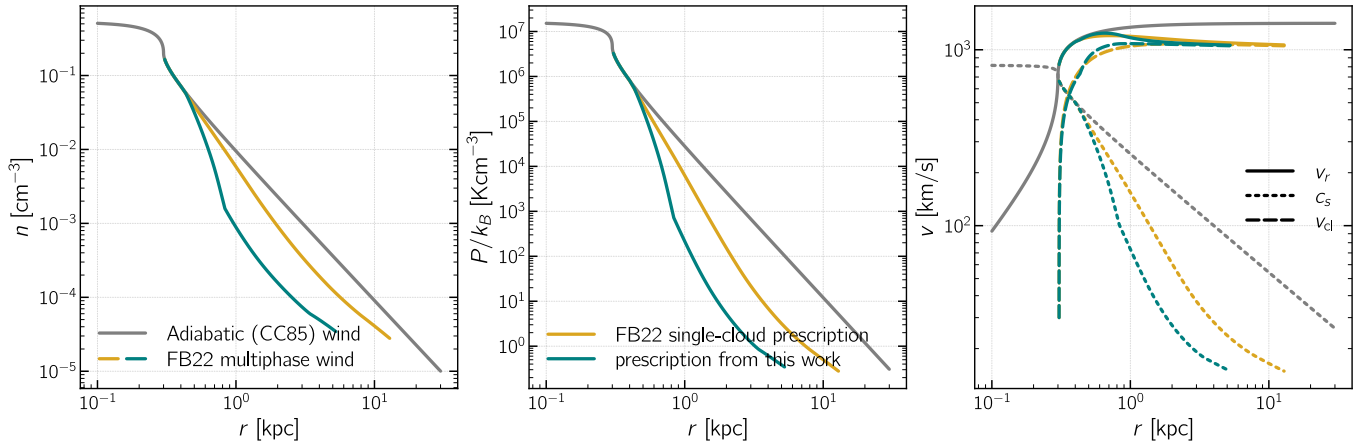


Figure 13. Comparison of the FB22 multiphase wind profile (density: **left**, pressure: **middle**, velocity: **right** panel) due to the modification to the underlying single-cloud evolution introduced in our work (in **blue**) with the original FB22 single-cloud model (in **orange**). The right panel shows different velocities, namely the wind speed v_r , the wind sound speed c_s , and the cloud speed v_{cl} as indicated in the legend attached to the figure. The wind parameters chosen for both the orange and blue lines are the same as that used in Fig. 6 from FB22 with an initial cloud mass of $100 M_\odot$ (corresponding to $\xi_{init} = 3.16$ in the original FB22 model and $\xi_{init} = 3.95$ in our prescription). The single-cloud model (cf. Fig. 12 & Eq. E1) that controls the mass and energy loading due to the multiphase mixing of clouds seeded in an outflow is different between the two models (in orange and blue). This highlights that the evolution of clouds in an outflow plays a crucial role in setting the large scale properties of their host outflow. These clouds become increasingly important as the efficiency of mass and energy loading in the wind increases. For reference, the **gray** lines show the classic single phase adiabatic wind profile (CC85). Follow the [link here](#) for a full image of all the relevant quantities similar to Fig. 6 from FB22.

multiphase wind obtained when switching to our modified single-phase cloud prescription, in blue (discussed at the beginning of this section). For reference, the solution for the single phase CC85 wind is shown in gray in the figure. The wind profiles (blue and orange lines in Fig. 13) differ substantially from one another ($\gtrsim 1$ dex) over a substantial downstream distance. In order to match the simulation results, our prescription has been tuned to produce a higher mass of cold gas formed in a CC85 wind compared to the original FB22 prescription (cf. Fig. 12). Consequently, the wind in our modified prescription has more mass loading by the clouds and its properties exhibit a greater deviation from the single-phase adiabatic wind – evident in the density, pressure, and velocity profiles for the wind (blue curves showing the original FB22 prescription are closer to the gray CC85 profile). As expected, the mass in cold clouds is higher in our prescription, which results in a higher loading of mass and energy in the cold phase of the multiphase wind. This is compensated by a lower mass and energy loading into the hot phase, which is introduced into the wind as the clouds get mixed and evaporated. The higher loading of cold gas from the clouds also results in a greater reduction of entropy from the constant CC85 entropy profile beyond the region where the clouds are injected. Since cloud evolution directly affects the mass and energy loading of an outflow and its multiphase nature, winds with higher efficiency of mass loading are increasingly affected by the behavior of an increased number of clouds that are seeded in them. Overall, our comparison highlights the need to accurately test the models of individual cloud-wind evolution in order to get an accurate model of multiphase galactic outflows.

4.2 Emission from clouds in a CC85 wind

The turbulent mixing layers and cooling flows surrounding the cold cloud radiate energy, powered by the enthalpy flux from the hot to the cold medium. In a steady state when a cloud is entrained, the bolometric luminosity is proportional to the mass flux. In a TRML or a local cooling flow, the total radiative cooling rate equals the enthalpy inflow rate (both proportional to the mass flux), which

is regulated by the density and temperature distribution within the cooling layer. Thus, because of the lower mass growth rates we found for clouds embedded in a CC85 wind compared to a uniform one (cf. Fig. 5 & Section 4.1.1), we expect the potentially observable surface brightness levels to be accordingly lower.

Another equivalent way to interpret this is that the surface brightness of the gas depends on its emissivity, which is proportional to the square of the gas density.⁹ Since the density of the cold gas formed due to cloud-crushing in an adiabatically expanding background keeps falling, its surface brightness is expected to be significantly diminished as the clouds move down the wind. In addition, the enthalpy flux and hence the emission can slightly differ from (the non-entrained, dense) head to (entrained, diffuse) tail, in both the homogeneous cloud-crushing and the CC85 wind because of the variation in density and \dot{m}_{cl} (cf. Tan et al. 2021). This is certainly not the case anymore once the cold cloud is fully entrained. Even in this state, our expanding wind setup still exhibits a strong emission gradient not present for clouds in a homogeneous background.

Fig. 14 shows the surface brightness of cold gas from our fiducial cloud-crushing simulation (cf. Table 1) at different times. To calculate the surface brightness map (projected in the z -direction orthogonal to the wind), we calculate $n_H^2 \Lambda(T) \Delta V$ for every cell in the simulation domain and add them along the z -direction, where ΔV is cell volume. The radiative loss for gas at the floor temperature is set to zero, i.e., $\Lambda(T_{cl}) = 0$. As the cloud moves in the wind, it expands, and its surface brightness diminishes, consistent with the above discussion. The insets with each of the surface brightness plots in Fig. 14 show a slice of emission rate per unit volume through the center of our simulation domain. These clearly demonstrate that emission is dominated by the radiatively cooling boundary layers between the cloud and the wind. Contributions from several such slices of emission have been integrated along the line of sight (z -axis, here) to

⁹ This is emissivity integrated across all wavelengths and might not be strictly valid for any individual emission lines like HI.

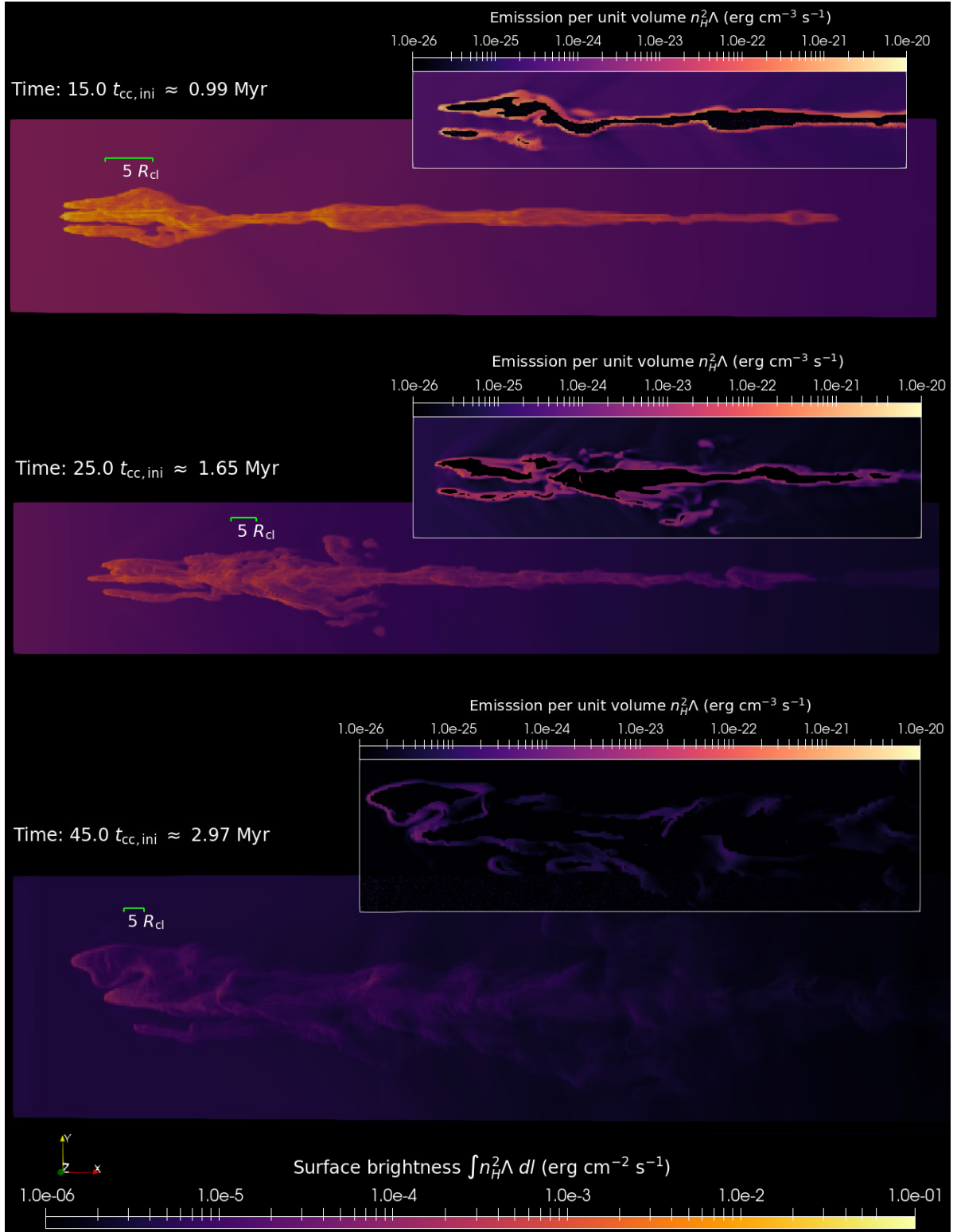


Figure 14. The temporal evolution of the total surface brightness from our cloud-crushing simulation in a CC85 wind using fiducial parameters $(\mathcal{M}, \chi, t_{\text{cool,mix}}/t_{\text{cc|ini}}) = (1.496, 100, 0.2)$; cf. Table 1. Here, we show only a few selected snapshots that clearly demonstrate the trend that the emissivity from the cloud gradually fades with time. This is due to the weakening of radiative cooling downstream leading to a reduction in the amount of dense, cold mass growing due to shear-driven mixing in the turbulent boundary layers between the cloud and the wind. The main body of the cloud is very close to the floor temperature of our simulation, at which the emission is set to zero. This is clearly demonstrated in the inset figures showing emissivity per unit volume of the gas on a slice passing through the center of our simulation domain with normal along the z -axis. Emission is dominated by the turbulent boundary layers. Similar layers are integrated along the z -axis to obtain the projected surface brightness plots in this figure. Note that the zoom levels are different across snapshots, indicated by the scales attached along with them.

generate the surface brightness maps. The bulk of the cloud is at the cooling floor of our simulation ($T = 4 \times 10^4$ K), emission from which is set to zero. Fig. 14 shows a strong gradient in surface brightness in the elongated tails of the cloud, with the surface brightness of the long cometary cloud tails dimming along the wind.

We point out that the surface brightness gradient in Fig. 14 is for an individual cloud. For a more realistic comparison, a semi-analytical wind model including several clouds (cf. Section 4.1.2) has to be convolved with the global surface brightness profile. Such wind models need to be multiphase by implicitly taking into account mass and energy loading by several such clouds. Comparing predicted and observed surface brightness maps is an interesting future avenue to constrain the models and our understanding of galactic winds. In particular, a statistical measure of emission gradients can reveal the properties of the hot medium otherwise inaccessible at higher redshifts.

The M82 galaxy is a classic example of a starburst-driven galaxy harboring strong outflows (Lynds & Sandage 1963), which we use as a benchmark for comparing simulation results. Clouds simulated in an expanding wind have a morphological similarity with the elongated cold gas ‘chimneys’ observed by Bolatto et al. 2024; Fisher et al. 2025 in the M82 galaxy. The infrared emission from the cold gas and dust observed using JWST in M82 by Bolatto et al. 2024; Fisher et al. 2025 is formed in a starburst-driven outflow environment, similar to what we have simulated. Long, elongated plumes of cold gas also show a similar gradient in their emission along the direction of the wind (see Figs. 4 & 6 from Fisher et al. 2025). As discussed earlier, such a strong gradient in the surface brightness of the cold clouds is not possible in ‘vanilla’ cloud-crushing because the clouds in homogeneous cloud-crushing setups lack differential expansion parallel to the wind due to the absence of a spatial gradient in the wind. It is worth noting that we are unable to reproduce the loop-like features towards the center of the wind, which are very likely magnetically dominated structures – beyond the scope of our pure hydro simulations. A detailed, quantitative comparison with the measured emission gradients can help us constrain the mass transfer rate between the phases, and in particular, study the hot, accelerated phase, which is otherwise inaccessible but crucial in order to constrain feedback models.

4.3 Caveats and Future Directions

The Chevalier & Clegg 1985 (CC85) model of an adiabatically expanding outflow makes dramatic simplifications. Observations show that the thermodynamic state of the outflowing gas can be significantly different from a steady CC85 wind (Xu et al. 2023). For instance, Lopez et al. 2020 observe much shallower density and temperature profiles (also in free electron density profile observed by Deanne Fisher; private communication) for the X-ray bright hot gas beyond 1 kpc in M82 compared to the CC85 model. Such deviations can be generic and wind profiles can potentially be non-steady in various starburst-driven outflows. Our work highlights that the expansion of the wind bears non-trivial implications for the survival/growth of cold clouds in outflows.¹⁰ This is not surprising, and depending on the background profile, clouds behave significantly differently in how

they mix, shred, or grow (cf. also Tan et al. 2023 for clouds infalling in a stratified medium).

An extensive study of the behavior of cold clouds in diverse astrophysically relevant environments under a unified framework has yet to be explored. Furthermore, the assumptions that go into the CC85 model, such as spherical symmetry and continuous energy and mass injection are extremely simplistic. Supernovae can be clustered or spread out in the galactic disk, and the injection of mass and energy by them can be in the form of bursty episodes (Schneider et al. 2020; Schneider & Mao 2024; Mohapatra et al. 2025), for which the outflow does not attain a smooth CC85 profile (Sharma et al. 2014). All of these effects can add additional complications, including driving a significant amount of turbulence in the wind (Ghosh et al.; in prep) and transport of metals (Sharda et al. 2024) that can potentially alter how the individual clouds or their population evolve in outflows. Therefore, different models of supernovae feedback (Warren et al. 2025) and turbulence give rise to a great deal of spatial and temporal variations in the background conditions (Mohapatra & Sharma 2019; Mohapatra et al. 2020) that different cold clouds encounter. These must be carefully taken into account before robust comparison can be made with observations and simulations (both large-scale outflow simulations of isolated galaxies; Schneider & Robertson 2017; Schneider et al. 2018, 2020; Kim & Ostriker 2018; Vijayan et al. 2018, 2020; Steinwandel et al. 2024; Wang et al. 2024; Li et al. 2025; Vijayan et al. 2025 or cosmological simulations of galaxy formation; Davé et al. 2020; Ramesh et al. 2024) of cold clouds and their host galactic winds. Although not directly related to the idealized simulations discussed here, similar caveats must be considered while testing the applicability of different sub-grid models of cold gas in cosmological simulations (Weinberger & Hernquist 2023; Smith et al. 2024a,b; Bennett et al. 2024; Butsky et al. 2024; Das et al. 2024) under various kinematic and thermodynamic conditions.

We make qualitative parallels of our cloud-crushing simulation results with recent JWST observations of infrared emission line maps (from cold clouds and dust) in the M82 outflow by Fisher et al. 2025. However, a detailed comparison would require cloud-crushing simulations to include the molecular phase ($\lesssim 10^4$ K) which brings in additional physics like self-gravity, self-shielding, dust sputtering and creation (Kannan et al. 2021; Girichidis et al. 2021; Farber & Gronke 2022; Chen & Oh 2024), which we have not taken into account.

In addition, the effects of thermal conduction and magnetic fields can be significant in determining the small-scale structure of cold clouds. Several recent works have demonstrated that magnetic fields suppress mixing-induced hydrodynamic instabilities, reducing the rate at which the cold mass grows in cloud-crushing simulations (McCourt et al. 2015; Kooij et al. 2021) – a picture also supported by recent idealized simulations of radiative turbulent mixing layers with magnetic fields by Das & Gronke 2024. Moreover, magnetic fields give rise to additional drag on the cloud due to draping by magnetic fields (Dursi & Pfrommer 2008) which is very sensitive to not just the magnetic field strength but more importantly to the orientation of the magnetic fields (Hidalgo-Pineda et al. 2024; Kaul et al. 2025) with respect to the direction of motion of the clouds or the direction of spatial gradients in the background medium. Strength and orientation of magnetic fields might also be responsible for the generation of cold filamentary structures observed in galactic outflows (like M82) that bear striking similarity with solar prominences. In systems similar to cloud-crushing, magnetic fields have also been found to modulate the properties of ram-pressure stripped tails in jellyfish galaxies (Müller et al. 2021). Therefore, magnetic fields and their associated effects can give rise to slow movement of long-lived

¹⁰ For instance, in an isothermally expanding wind, we expect a significantly reduced cloud mass growth than in an adiabatically expanding wind. From our analytic considerations, we expect $m_{\text{cl}} \propto d_{\text{cl}}^{1/4}$ in an isothermal wind (not validated against any simulations carried out in this paper).

clouds, leading to higher cold-mass seeding at any position in the bulk of the outflow, albeit at a lower rate. Furthermore, a distribution of multiple clouds (common in the CGM; cf. Liang & Remming 2020; Singh Bisht et al. 2024; Hummels et al. 2024; Tan & Fielding 2024) can interact with each other (Nguyen et al. 2024) and can also change the bulk properties of the wind by inducing precipitation (owing to thermal instability; Thompson et al. 2016; Schneider et al. 2018; Dannen et al. 2020; Lochhaas et al. 2021). Such effects can give rise to multiphase outflows with significantly different kinematic and thermodynamic properties, not considered in our work. Careful consideration of such effects and their relative importance and diverse outflow environments should be considered in the future. This would enable simulations to make realistic predictions of cloud properties in different regimes and bridge the discrepancies between predictions from small-scale simulations and results of large-scale simulations of individual galaxies or cosmological simulations.

Other HST observations and analysis of cool clouds (bright in $H\alpha$) in M82 outflow reveal that their properties (like density contrast, size, pressure and cooling times) are comparable to the clouds in cloud-crushing simulations (Mutchler et al. 2007; Thompson & Heckman 2024). However, a significant amount of work needs to be done to explain the detailed morphology of these observed structures. In particular, a large fraction of these observed clouds seem to be immersed in an inherently turbulent medium (Lv et al. 2024) and form arc-like structures (Lopez et al. 2025) that lack the distinct comet-like head-tail morphology predicted by cloud-crushing simulations. Moreover, even for predicting the emissivity or column densities of certain ions tracing the cold gas (like NV) from simulations, one might need to consider not just extra-galactic sources, but additional sources of photo-ionizing UV background radiation from stars, especially when the star formation rate is very high, like in M82 (Villarruel et al. 2024). Additional photo-heating can also be dynamically important in determining the cooling rates in the turbulent radiative mixing layers (TRMLs) as well as the multiphase nature of the galactic winds that host them (Sarkar et al. 2022).

Despite all these caveats, the expansion of galactic outflows is expected to be generic and we expect our simulation results to be a qualitative indicator of cloud properties in multiphase outflow environments.

5 SUMMARY & CONCLUSION

The formation and survival of cold clouds in galactic outflows are crucial for explaining the ubiquity of cold gas in the CGM. Observations suggest that cold clouds are accelerated farther from the galactic disk by powerful bursts of supernovae. The outflowing gas is routinely found to have an expansion in the wind away from the center of the galactic disk. In this work, we simulate the evolution of cold clouds seeded in an expanding wind, which is modeled by a steady-state Chevalier & Clegg 1985 (CC85) profile. The adiabatically expanding outflow shreds, stretches, and mixes the cold clouds seeded in the wind. In general, we find that

(i) Compared to the indefinite growth of cold mass seen in ‘vanilla’ cloud crushing simulations (Brüggen & Scannapieco 2016; Armillotta et al. 2017; Gronke & Oh 2018; Li et al. 2020; Sparre et al. 2020; Kanjilal et al. 2021; Abruzzo et al. 2023), clouds with the same initial condition but exposed to a steady adiabatically expanding (CC85) wind, instead of a uniform wind, undergo significantly lower cold mass growth (can be lower by almost an order of magnitude; see Fig. 5).

(ii) As a cloud travels down the CC85 wind, it expands, becomes roughly isobaric relative to the local wind, and its properties depend on its instantaneous position in the wind (see Fig. 6). The cloud maintains ‘local’ pressure equilibrium with the wind. This causes it to continuously lose its density contrast with the wind proportional to the distance travelled $d_{cl}^{-2\gamma}$ by it. Eventually, the cloud fades in the background wind and become indistinguishable from its surroundings (see Fig. 7) – a picture also supported by the evolution of the phase space distribution of cloud pressure and density (see Fig. 8).

(iii) We find that the expansion associated with the CC85 wind results in clouds embedded in them to spread in directions orthogonal to the wind. Once entrained, the cloud expansion is proportional to the distance travelled by the cloud d_{cl} (see Fig. 9), and the cold gas mass m_{cl} grows proportional to the square of the distance they travel, i.e., $m_{cl} \propto d_{cl}^2$ (for entrained clouds; see Fig. 10). This also explains the suppression of cold mass growth compared to the uniform wind ‘vanilla’ cloud-crushing, where $m_{cl} \propto d_{cl}^3$ – a significantly steeper cold mass growth with distance.

(iv) We compare our simulation results with the prediction of the phenomenological model of single-cloud evolution in galactic outflows proposed by Fielding & Bryan 2022 (FB22; Section 3 in their paper). Upon comparing cloud mass growth with time with our simulations using the parameters chosen for their model (Section 3.2 in their paper), we are unable to reproduce the suppression of cold mass growth in a CC85 wind compared to their ‘vanilla’ cloud-crushing counterparts (uniform wind) for all our simulation parameters. The FB22 model is very sensitive to the fractal dimension of the radiatively cooling turbulent boundary layer, which can be tweaked to match our simulation result (see Fig. 12). This highlights that the treatment of an individual cloud evolution in FB22 (Section 3.1 in their paper) is generic and can potentially be improved to match simulation results in future. However, this is not robust across different simulation parameters and further work is needed towards developing a sound physical interpretation of any specific choice of single-cloud evolution model. FB22 also developed a general framework for the profile of a multiphase outflow (equations in Fig. 3 & Eq. 17 in FB22) with different energy and mass source terms in the wind. These source terms can come from any model of single cloud evolution in galactic outflows. In particular, we introduce source terms to account for the cloud-wind interaction from the phenomenological cloud-crushing model that we discussed earlier. Using the general multiphase wind framework from FB22, we find that changes in the behavior of individual clouds in the wind lead to substantial changes in the global properties of their host outflow (see Fig. 13). This has important implications for enhancing the applicability of the FB22 model as a sub-grid prescription across the diverse range of conditions typically encountered in cosmological simulations – one of the primary motivations for developing such models.

(v) We estimate the surface brightness of the clouds in our expanding cloud-crushing simulations (see Fig. 14). We find that, just like in the ‘vanilla’ cloud-crushing, most of the emission is confined to the radiatively cooling mixing layers. However, the mixing layers gradually become lower in density as the cloud encounters a lower-density wind in an adiabatically expanding outflow. Therefore, the surface brightness of the cloud continues to drop and they gradually become indistinguishable from the background. In addition, the surface brightness of the cold cloud shows a gradient that gradually dims downstream of the wind. This feature bears a striking resemblance to the recent JWST observation of the cold-cloud emission map in the outflow of M82 (Fisher et al. 2025).

We hope that this study will be a stepping stone in our effort to

bridge the gap between idealized simulations and the complex, multiphase nature of real galactic winds. A great deal of work is still needed to generalize the behavior of cold clouds in diverse environments and constrain their collective effect on large-scale properties of their host outflows so that simulations and models can faithfully reproduce current and upcoming observations.

ACKNOWLEDGEMENTS

AD acknowledges support from the Max-Planck-Gesellschaft. AD acknowledges his colleague Ayan Ghosh for helping with the cartoon illustration used in this paper. AD also expresses his gratitude to his colleague Ritoli Ghosh for help with visualizations and also for several hours of useful discussions. AD also acknowledges Arif Babul, Kartick Sarkar, Evan Scannapieco Matthew Abruzzo, Volker Springel, Evan Schneider, Christoph Pfrommer, Tiago Costa, Filippo Fraternali, Greg Bryan, Rainer Weinberger, Ruediger Pakmor, Matthew Smith, Sunmyon Chon, Drummond Fielding, and Simon White for their useful comments and discussions. The authors acknowledge support from the Supercomputer Education and Research Center (SERC) at the Indian Institute of Science (IISc), Bangalore, where some of the production runs of our simulations were carried out. AD would like to express his gratitude to the super-responsive and helpful people at [Paraview forum](#) for all the technical support needed for some of the visualizations. Research of AD as a graduate student, when a significant part of this paper was written, was supported by the Prime Minister's Research Fellowship (PMRF) from the Ministry of Education (MoE), Govt. of India. AD acknowledges the support from the Max Planck Institute for Astrophysics, Garching, for accepting him as a visiting student and providing access to their Freya & Orion supercomputing clusters when this work was initiated. Several analysis scripts in our work make use of Numpy ([Harris et al. 2020](#)), Matplotlib ([Hunter 2007](#)), and Scipy ([Virtanen et al. 2020](#)) whose communities we thank for continued development and support. MG thanks the Max Planck Society for support through the MPRG.

6 DATA AVAILABILITY

All the relevant data associated with this article will be shared on a reasonable request to the authors. Most of the relevant plotting and visualization codes are hosted on GitHub for public access. Follow <https://github.com/dutta-alankar/CCinCC85/> for cloud-crushing in spherical CC85 wind simulations and `exp_box` branch in https://github.com/dutta-alankar/cloud-crushing_PLUTO/tree/exp_box where reimplementation of the expanding box simulation by [Gronke & Oh 2020](#) has been done.

REFERENCES

- Abruzzo M. W., Fielding D. B., Bryan G. L., 2023, [arXiv e-prints](#), p. [arXiv:2307.03228](#)
- Abruzzo M. W., Fielding D. B., Bryan G. L., 2024, [ApJ](#), **966**, 181
- Alf uzas R., Pittard J. M., Hartquist T. W., Falle S. A. E. G., Langton R., 2012, [MNRAS](#), **425**, 2212
- Angl es-Alc azar D., Faucher-Gigu ere C.-A., Quataert E., Hopkins P. F., Feldmann R., Torrey P., Wetzel A., Kere  D., 2017, [MNRAS](#), **472**, L109
- Antolin P., 2020, [Plasma Physics and Controlled Fusion](#), **62**, 014016
- Antolin P., Shibata K., Vissers G., 2010, [ApJ](#), **716**, 154
- Armillotta L., Fraternali F., Marinacci F., 2016, [MNRAS](#), **462**, 4157
- Armillotta L., Fraternali F., Werk J. K., Prochaska J. X., Marinacci F., 2017, [MNRAS](#), **470**, 114
- Aung H., Mandelker N., Dekel A., Nagai D., Semenov V., van den Bosch F. C., 2024, [MNRAS](#), **532**, 2965
- Barenblatt G. I., Zel'dovich Y. B., 1972, [Annual Review of Fluid Mechanics](#), **4**, 285
- Begelman M. C., Fabian A. C., 1990, [Monthly Notices of the Royal Astronomical Society](#), **244**, 26
- Belli S., et al., 2024, [Nature](#), **630**, 54
- Benjamin R. A., Danly L., 1997, [ApJ](#), **481**, 764
- Bennett J. S., Smith M. C., Fielding D. B., Bryan G. L., Kim C.-G., Springel V., Hernquist L., 2024, [arXiv e-prints](#), p. [arXiv:2410.12909](#)
- Berlok T., Pfrommer C., 2019, [MNRAS](#), **489**, 3368
- Binney J., Nipoti C., Fraternali F., 2009, [MNRAS](#), **397**, 1804
- Bolato A. D., et al., 2024, [ApJ](#), **967**, 63
- Bregman J. N., 1980, [ApJ](#), **236**, 577
- Br uggen M., Scannapieco E., 2016, [ApJ](#), **822**, 31
- Butsky I. S., Hummels C. B., Hopkins P. F., Quinn T. R., Werk J. K., 2024, [MNRAS](#), **535**, 1672
- Campitiello M. G., et al., 2021, [ApJ](#), **911**, 144
- Chen Z., Oh S. P., 2024, [MNRAS](#), **530**, 4032
- Chevalier R. A., Clegg A. W., 1985, [Letters to Nature](#), 0563
- Choudhury P. P., Sharma P., Quataert E., 2019, [MNRAS](#), **488**, 3195
- Cole S., Aragon-Salamanca A., Frenk C. S., Navarro J. F., Zepf S. E., 1994, [MNRAS](#), **271**, 781
- D'Onghia E., Fox A. J., 2016, [ARA&A](#), **54**, 363
- Dannen R. C., Proga D., Waters T., Dyda S., 2020, [ApJ](#), **893**, L34
- Das H. K., Gronke M., 2024, [MNRAS](#), **527**, 991
- Das H. K., Gronke M., Weinberger R., 2024, [arXiv e-prints](#), p. [arXiv:2412.03751](#)
- Dav e R., Crain R. A., Stevens A. R. H., Narayanan D., Saintonge A., Catinella B., Cortese L., 2020, [MNRAS](#), **497**, 146
- Davies J. J., Crain R. A., Oppenheimer B. D., Schaye J., 2020, [MNRAS](#), **491**, 4462
- Deb T., et al., 2022, [MNRAS](#), **516**, 2683
- Dekel A., Silk J., 1986, [ApJ](#), **303**, 39
- Dekel A., et al., 2009, [Nature](#), **457**, 451
- Dursi L. J., Pfrommer C., 2008, [ApJ](#), **677**, 993
- Dutta A., Sharma P., 2019, [Research Notes of the AAS](#), **3**, 148
- Dutta A., Sharma P., Nelson D., 2022, [MNRAS](#), **510**, 3561
- Erb D. K., 2008, [ApJ](#), **674**, 151
- Farber R. J., Gronke M., 2022, [MNRAS](#), **510**, 551
- Faucher-Gigu ere C.-A., Oh S. P., 2023, [ARA&A](#), **61**, 131
- Federrath C., Klessen R. S., Schmidt W., 2009, [ApJ](#), **692**, 364
- Fielding D. B., Bryan G. L., 2022, [ApJ](#), **924**, 82
- Fielding D. B., Ostriker E. C., Bryan G. L., Jermyn A. S., 2020, [The Astrophysical Journal](#), **894**, L24
- Fisher D. B., et al., 2025, [MNRAS](#), **538**, 3068
- Fluetsch A., et al., 2021, [MNRAS](#), **505**, 5753
- Fox A. J., Frazer E. M., Bland-Hawthorn J., Wakker B. P., Barger K. A., Richter P., 2020, [ApJ](#), **897**, 23
- Franchetto A., et al., 2020, [ApJ](#), **895**, 106
- Fraternali F., 2009, in Andersen J., Nordstr ora m B., Bland-Hawthorn J., eds, [IAU Symposium Vol. 254, The Galaxy Disk in Cosmological Context](#). pp 255–262 ([arXiv:0807.3365](#)), [doi:10.1017/S1743921308027671](#)
- Fraternali F., 2017, in Fox A., Dav e R., eds, [Astrophysics and Space Science Library Vol. 430, Gas Accretion onto Galaxies](#). p. 323 ([arXiv:1612.00477](#)), [doi:10.1007/978-3-319-52512-9_14](#)
- Fraternali F., Binney J. J., 2008, [MNRAS](#), **386**, 935
- Ghosh R., Dutta A., Sharma P., 2024, [MNRAS](#), **531**, 3445
- Girichidis P., Naab T., Walch S., Berlok T., 2021, [MNRAS](#), **505**, 1083
- Gronke M., Oh S. P., 2018, [MNRAS](#), **480**, L111
- Gronke M., Oh S. P., 2020, [MNRAS](#), **492**, 1970
- Haardt F., Madau P., 2012, [ApJ](#), **746**, 125
- Harris C. R., et al., 2020, [Nature](#), **585**, 357
- Heckman T. M., Armus L., Miley G. K., 1990, [ApJS](#), **74**, 833

- Heckman T. M., Lehnert M. D., Strickland D. K., Armus L., 2000, *ApJS*, **129**, 493
- Heitsch F., Putman M. E., 2009, *ApJ*, **698**, 1485
- Heller V., 2017, *Journal of Hydraulic Research*, **55**, 293
- Hidalgo-Pineda F., Farber R. J., Gronke M., 2024, *MNRAS*, **527**, 135
- Hillier A., Oliver R., Martínez-Gómez D., 2025, *A&A*, **696**, A231
- Hopkins P. F., Quataert E., Murray N., 2012, *MNRAS*, **421**, 3522
- Houck J. C., Bregman J. N., 1990, *ApJ*, **352**, 506
- Hummels C. B., Rubin K. H. R., Schneider E. E., Fielding D. B., 2024, *ApJ*, **972**, 148
- Hunter J. D., 2007, *Computing in Science & Engineering*, **9**, 90
- Ji S., Oh S. P., Masterson P., 2019, *MNRAS*, **487**, 737
- Jun B.-I., Jones T. W., Norman M. L., 1996, *ApJ*, **468**, L59
- Kanjilal V., Dutta A., Sharma P., 2021, *MNRAS*, **501**, 1143
- Kannan R., Vogelsberger M., Marinacci F., Sales L. V., Torrey P., Hernquist L., 2021, *Monthly Notices of the Royal Astronomical Society*, **503**, 336
- Kaul I., Tan B., Oh S. P., Mandelker N., 2025, *MNRAS*, **539**, 3669
- Kavvas M. L., Ercan A., 2016, in AGU Fall Meeting Abstracts. pp NG11A–01
- Keller B. W., Kruijssen J. M. D., Wadsley J. W., 2020, *MNRAS*, **493**, 2149
- Kereš D., Katz N., Weinberg D. H., Davé R., 2005, *MNRAS*, **363**, 2
- Kim C.-G., Ostriker E. C., 2018, *ApJ*, **853**, 173
- Klein R., Mckee C., Colella P., 1994, *The Astrophysical Journal*, **420**, 213
- Kolotkov D. Y., Antolin P., Sharma P., 2023, *Front. Astron. Space Sci.*, **10**
- Kooij R., Grønnow A., Fraternali F., 2021, *MNRAS*, **502**, 1263
- Lehner N., Howk J. C., Marasco A., Fraternali F., 2022, *MNRAS*, **513**, 3228
- Lehnert M. D., Heckman T. M., 1996, *ApJ*, **472**, 546
- Li Z., Hopkins P. F., Squire J., Hummels C., 2020, *MNRAS*, **492**, 1841
- Li A., Fraternali F., Marasco A., Trager S. C., Pezzulli G., Mancera Piña P. E., Verheijen M. A. W., 2023, *MNRAS*, **520**, 147
- Li X.-F., Zhu W., Wang T.-R., Feng L.-L., 2025, *ApJ*, **982**, 28
- Liang C. J., Remming I., 2020, *MNRAS*, **491**, 5056
- Lochhaas C., Thompson T. A., Schneider E. E., 2021, *MNRAS*, **504**, 3412
- Lopez L. A., Mathur S., Nguyen D. D., Thompson T. A., Olivier G. M., 2020, *ApJ*, **904**, 152
- Lopez S., Lopez L. A., Thompson T. A., Leroy A. K., Bolatto A. D., 2025, *arXiv e-prints*, p. [arXiv:2502.06934](https://arxiv.org/abs/2502.06934)
- Lucchini S., D’Onghia E., Fox A. J., 2021, *ApJ*, **921**, L36
- Lv A., Wang L., Cen R., Ho L. C., 2024, *ApJ*, **977**, 274
- Lynds C. R., Sandage A. R., 1963, *ApJ*, **137**, 1005
- Mandelbrot B. B., 1975, *Journal of Fluid Mechanics*, **72**, 401
- Mandelker N., Padnos D., Dekel A., Birnboim Y., Burkert A., Krumholz M. R., Steinberg E., 2016, *MNRAS*, **463**, 3921
- Mandelker N., Nagai D., Aung H., Dekel A., Padnos D., Birnboim Y., 2019, *MNRAS*, **484**, 1100
- Mandelker N., Nagai D., Aung H., Dekel A., Birnboim Y., van den Bosch F. C., 2020, *MNRAS*, **494**, 2641
- Marasco A., Fraternali F., Lehner N., Howk J. C., 2022, *MNRAS*, **515**, 4176
- Marinacci F., Binney J., Fraternali F., Nipoti C., Ciotti L., Londrillo P., 2010, *MNRAS*, **404**, 1464
- Marinacci F., Fraternali F., Nipoti C., Binney J., Ciotti L., Londrillo P., 2011, *MNRAS*, **415**, 1534
- Martin D. C., et al., 2019, *Nature Astronomy*, **3**, 822
- McCourt M., Sharma P., Quataert E., Parrish I. J., 2012, *MNRAS*, **419**, 3319
- McCourt M., O’Leary R. M., Madigan A.-M., Quataert E., 2015, *MNRAS*, **449**, 2
- McQuinn M., Werk J. K., 2018, *ApJ*, **852**, 33
- Mignone A., Bodo G., Massaglia S., Matsakos T. and Tesileanu O., Zanni C., Ferrari A., 2007, *The Astrophysical Journal Supplement Series*, **170**, 228
- Mishra S., et al., 2024, *ApJ*, **976**, L28
- Mohapatra R., Sharma P., 2019, *MNRAS*, **484**, 4881
- Mohapatra R., Federrath C., Sharma P., 2020, *MNRAS*, **493**, 5838
- Mohapatra R., Federrath C., Sharma P., 2022, *MNRAS*, **514**, 3139
- Mohapatra R., Quataert E., Fielding D., Guo M., 2025, *arXiv e-prints*, p. [arXiv:2502.05329](https://arxiv.org/abs/2502.05329)
- Müller A., Ignesti A., Poggianti B., Moretti A., Ramatsoku M., Dettmar R.-J., 2021, *Galaxies*, **9**, 116
- Mutchler M., et al., 2007, *PASP*, **119**, 1
- Naab T., Ostriker J. P., 2017, *ARA&A*, **55**, 59
- Nakamura F., McKee C. F., Klein R. I., Fisher R. T., 2006, *ApJS*, **164**, 477
- Nelson D., et al., 2020, *MNRAS*, **498**, 2391
- Nguyen D. D., Thompson T. A., Schneider E. E., Tarrant A. P., 2024, *MNRAS*, **531**, 1338
- Nikolis C., Gronke M., 2024, *MNRAS*, **530**, 4597
- Oosterloo T., Fraternali F., Sancisi R., 2007, *AJ*, **134**, 1019
- Oppenheimer B. D., et al., 2020, *MNRAS*, **491**, 2939
- Orlando S., Peres G., Reale F., Bocchino F., Rosner R., Plewa T., Siegel A., 2005, *A&A*, **444**, 505
- Pezzulli G., Fraternali F., 2016, *MNRAS*, **455**, 2308
- Pittard J. M., Dyson J. E., Falle S. A. E. G., Hartquist T. W., 2005, *MNRAS*, **361**, 1077
- Poggianti B. M., et al., 2019, *ApJ*, **887**, 155
- Poludnenko A. Y., Frank A., Blackman E. G., 2002, *ApJ*, **576**, 832
- Putman M. E., 1999, *arXiv e-prints*, pp astro-ph/9909080
- Putman M. E., et al., 2002, *AJ*, **123**, 873
- Putman M. E., Peek J. E. G., Joung M. R., 2012, *ARA&A*, **50**, 491
- Ramatsoku M., et al., 2020, *A&A*, **640**, A22
- Ramesh R., Nelson D., 2024, *MNRAS*, **528**, 3320
- Ramesh R., Nelson D., Fielding D., Brüggem M., 2024, *arXiv e-prints*, p. [arXiv:2407.00172](https://arxiv.org/abs/2407.00172)
- Richter P., et al., 2017, *A&A*, **607**, A48
- Roberts-Borsani G. W., 2020, *MNRAS*, **494**, 4266
- Roberts I. D., et al., 2022, *ApJ*, **941**, 77
- Roediger E., Brüggem M., 2007, *MNRAS*, **380**, 1399
- Roy M., Su K.-Y., Tonnesen S., Fielding D. B., Faucher-Giguère C.-A., 2024, *MNRAS*, **527**, 265
- Rubin K. H. R., et al., 2022, *ApJ*, **936**, 171
- Sarkar K. C., 2024, *A&ARv*, **32**, 1
- Sarkar K. C., Sternberg A., Gnat O., 2022, *ApJ*, **940**, 44
- Scannapieco E., 2017, *ApJ*, **837**, 28
- Scannapieco E., Brüggem M., 2015, *ApJ*, **805**, 158
- Schiano A. V. R., Christiansen W. A., Knerr J. M., 1995, *ApJ*, **439**, 237
- Schneider E. E., Mao S. A., 2024, *ApJ*, **966**, 37
- Schneider E. E., Robertson B. E., 2017, *ApJ*, **834**, 144
- Schneider E. E., Robertson B. E., Thompson T. A., 2018, *ApJ*, **862**, 56
- Schneider E. E., Ostriker E. C., Robertson B. E., Thompson T. A., 2020, *ApJ*, **895**, 43
- Shapiro P. R., Field G. B., 1976, *ApJ*, **205**, 762
- Sharda P., Ginzburg O., Krumholz M. R., Forbes J. C., Wisnioski E., Mingozzi M., Zovaro H. R. M., Dekel A., 2024, *MNRAS*, **528**, 2232
- Sharma P., McCourt M., Quataert E., Parrish I. J., 2012, *MNRAS*, **420**, 3174
- Sharma P., Roy A., Nath B. B., Shchekinov Y., 2014, *MNRAS*, **443**, 3463
- Shin M.-S., Stone J. M., Snyder G. F., 2008, *ApJ*, **680**, 336
- Singh Bisht M., Sharma P., Dutta A., Nath B. B., 2024, *arXiv e-prints*, p. [arXiv:2411.17173](https://arxiv.org/abs/2411.17173)
- Smith M. C., et al., 2024a, *MNRAS*, **527**, 1216
- Smith M. C., Fielding D. B., Bryan G. L., Bennett J. S., Kim C.-G., Ostriker E. C., Somerville R. S., 2024b, *MNRAS*, **535**, 3550
- Sparre M., Pfrommer C., Ehlert K., 2020, *MNRAS*, **499**, 4261
- Sreenivasan K. R., Ramshankar R., Meneveau C., 1989, *Proceedings of the Royal Society of London Series A*, **421**, 79
- Steinhauser D., Schindler S., Springel V., 2016, *A&A*, **591**, A51
- Steinwandel U. P., Kim C.-G., Bryan G. L., Ostriker E. C., Somerville R. S., Fielding D. B., 2024, *ApJ*, **960**, 100
- Tan B., Fielding D. B., 2024, *MNRAS*, **527**, 9683
- Tan B., Oh S. P., Gronke M., 2021, *MNRAS*, **502**, 3179
- Tan B., Oh S. P., Gronke M., 2023, *Monthly Notices of the Royal Astronomical Society*, **520**, 2571
- Thompson T. A., Heckman T. M., 2024, *ARA&A*, **62**, 529
- Thompson T. A., Quataert E., Zhang D., Weinberg D. H., 2016, *MNRAS*, **455**, 1830
- Tonnesen S., Bryan G. L., 2010, *ApJ*, **709**, 1203
- Tonnesen S., Bryan G. L., 2012, *MNRAS*, **422**, 1609
- Tumlinson J., Peebles M. S., Werk J. K., 2017, *Annual Review of Astronomy and Astrophysics*, **55**, 389
- Veilleux S., Maiolino R., Bolatto A. D., Aalto S., 2020, *A&ARv*, **28**, 2
- Vietri M., Ferrara A., Miniati F., 1997, *ApJ*, **483**, 262

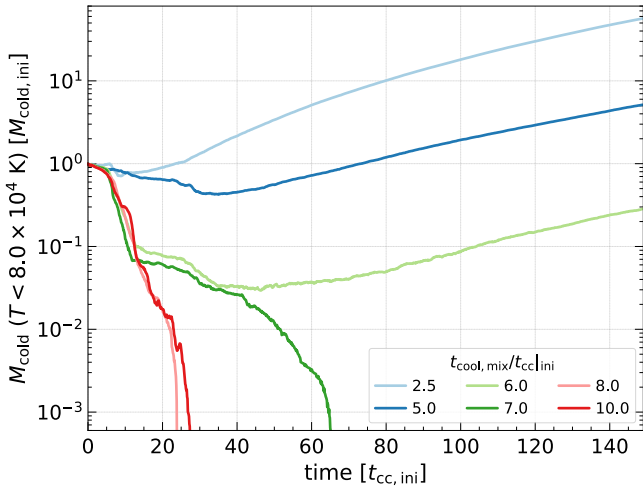


Figure A1. The temporal evolution of cold and dense gas mass (in units of initial mass) in our ‘vanilla’ cloud-crushing simulations (in spherical coordinates) for clouds of different sizes. The background wind is uniform and plane-parallel. In the simulations, cold and dense gas is identified as gas cells with a temperature lower than $2T_{cl} = 8 \times 10^4$ K. The set of constant parameters chosen for these simulations is $(M, \chi) = (1.496, 100)$. The parameter $t_{cool, mix}/t_{cc} \propto R_{thres}/R_{cl}$ is set to different values by changing the cloud size. Time is normalized by the cloud crushing time $t_{cc} = \sqrt{\chi} R_{cl}/v_{wind}$. This plot shows that the transition from destruction to the growth regime takes place at $t_{cool, mix}/t_{cc} \lesssim 6$ giving the dimensionless parameter $\delta \approx 6$ in Eq. 1.1.

- Vijayan A., Sarkar K. C., Nath B. B., Sharma P., Shchekinov Y., 2018, *MNRAS*, **475**, 5513
- Vijayan A., Kim C.-G., Armillotta L., Ostriker E. C., Li M., 2020, *ApJ*, **894**, 12
- Vijayan A., Krumholz M. R., Wibking B. D., 2025, *MNRAS*, **539**, 1706
- Villarruel D., Banda-Barragán W. E., Casavecchia B., 2024, *arXiv e-prints*, p. arXiv:2411.08704
- Vinod A., Kulkarni T., Bissetti F., 2024, *Proceedings of the Combustion Institute*, **40**, 105694
- Virtanen P., et al., 2020, *Nature Methods*, **17**, 261
- Voit M., 2018, in 42nd COSPAR Scientific Assembly. pp D2.2–1–18
- Vulcani B., et al., 2018, *ApJ*, **866**, L25
- Wakker B. P., 2001, *ApJS*, **136**, 463
- Wang B., 1995, *ApJ*, **444**, 590
- Wang T.-R., Zhu W., Li X.-F., Hong W.-S., Feng L.-L., 2024, *arXiv e-prints*, p. arXiv:2412.09452
- Warren O., Schneider E. E., Mao S. A., Abruzzo M. W., 2025, *ApJ*, **984**, 191
- Weinberger R., Hernquist L., 2023, *MNRAS*, **519**, 3011
- Wibking B. D., Voit G. M., O’Shea B. W., 2025, *MNRAS*, **537**, 739
- Xu J., Stone J. M., 1995, *ApJ*, **454**, 172
- Xu X., Heckman T., Yoshida M., Henry A., Ohya Y., 2023, *ApJ*, **956**, 142
- Yang Y., Ji S., 2023, *MNRAS*, **520**, 2148
- Zabl J., et al., 2020, *MNRAS*, **492**, 4576
- Zhang D., Thompson T. A., Quataert E., Murray N., 2017, *MNRAS*, **468**, 4801
- van de Voort F., Schaye J., Altay G., Theuns T., 2012, *MNRAS*, **421**, 2809

APPENDIX A: THRESHOLD SIZE FOR CLOUD MASS GROWTH IN A UNIFORM WIND

We carry out cloud-crushing simulation in a uniform plane parallel wind in spherical coordinates (‘vanilla’ cloud-crushing) for different cloud sizes to numerically evaluate the dimensionless parameter δ in Eq. 1.1. Fig. A1 shows that the transition from growing clouds to destroyed clouds (and vice versa) occurs at $t_{cool, mix}/t_{cc}|_{ini} \approx$

$R_{thres}/R_{cl} \approx 6$, where the symbols have their usual meaning. We have used this numerically determined threshold to choose different cloud sizes in all the simulations presented in this paper. Such a calibration is necessary because of slight differences in the cooling function and other parameters in various existing radiative cloud crushing simulations.

APPENDIX B: CLOUD SURFACE & SCALING RELATIONS

We investigate how the surface area scales with the volume of the cold gas in a CC85 wind. From geometric considerations, the cloud surface area A_{cl} should follow $A_{cl} \propto V_{cl}^{2/3}$, where V_{cl} is the volume of the cold cloud. This scaling relation is highlighted in a yellow band in the upper panel of Fig. B1, which shows that as clouds start to grow with strong radiative cooling, their surface area follows the simple geometric (non-fractal) scaling relation.

We also calculate the (mass) average inflow velocity v_{in} across the surface of the cold gas at different instants as a function of the center-of-mass of the cloud d_{cl} with respect to the initial position. To calculate this inflow velocity, we identify the iso-surface bounding all gas below $2T_{cl} = 8 \times 10^4$ K and calculate the local normal for every tile in the tessellation of the iso-surface. The inflow velocity v_{in} is the mass averaged velocity along the local normal for all the tiles bounding the iso-surface (see Abruzzo et al. 2024 for details). This inflow velocity v_{in} , although employing different definitions, was previously shown by Fielding et al. 2020; Gronke & Oh 2020; Tan et al. 2021 to follow the scaling relation $v_{in} \propto t_{cool, cl}^{-1/4}$ in the strong cooling regime, where $t_{cool, cl}$ is the cooling time of the cold gas – the fastest cooling phase. Using Eq. 3.1 and the arguments presented in Section 3.3 (that clouds are at T_{cl} and locally isobaric), we get $t_{cool, cl} \propto d_{cl}^{2\gamma}$. Therefore, the inflow velocity v_{in} follows $v_{in} \propto d_{cl}^{-\gamma/2}$, as indicated by the yellow band in Fig. B2. There is a significant scatter in the simulation data and this trend is only crudely followed by the clouds. The dependence of $R_{cl, \perp}$ ($\sim d$ (see Section 4.1.1) introduces a weak additional dependence of v_{in} ($\sim R_{cl, \perp}^{1/4} t_{cool, cl}^{-1/4} \sim d^{1/4 - \gamma/2} \approx d^{-\gamma/2}$; $\gamma = 5/3$) on the distance travelled by the cloud, which is even shallower but difficult to tell apart due to the noisy nature of v_{in} .

APPENDIX C: CLOUDS IN AN ANISOTROPICALLY EXPANDING BOX

Gronke & Oh 2020 (GO20 hereafter) employed a model of a homogeneous anisotropically expanding computational domain to approximate the evolution of a cloud in a CC85 wind. The cloud is assumed to be much smaller than its from the wind center. In addition, the entire cloud is assumed to experience a uniform wind condition, which only changes over time as the cloud moves down the wind. We re-simulated the cloud-crushing problem with the anisotropic expansion model used by GO20 in PLUTO for our fiducial parameters and ran it up to $30 t_{cc, ini}$. The extent of the simulation domain is $250R_{cl}$ in the direction of the wind and $22R_{cl}$ in directions orthogonal to it. Along with that, we utilize the frame boost method from Kanjilal et al. 2021 to track the cloud.

Comparing the evolution of clouds from our simulation and from GO20, we find that the simplifying assumptions made by GO20 lead to significant differences in the morphology of the cloud formed in the wind (see Fig. 11). We use identical initial conditions and resolution ($R_{cl}/d_{cell}|_{ini} = 16$) in both the simulation setups. As illustrated in

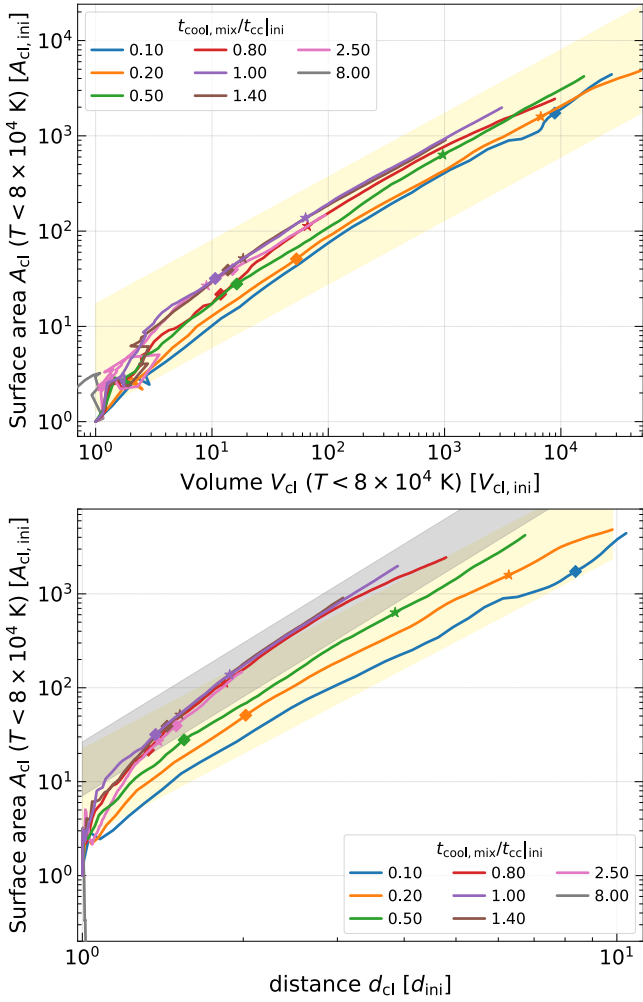


Figure B1. Evolution of the surface area (in units of the initial cloud surface area) of the radiatively cooling turbulent boundary layer, identified as the bounding surface of all gas below a temperature of $2T_{\text{cl}} = 8 \times 10^4$ K, as a function of cloud volume (**upper panel**) the distance (**lower panel**) travelled by the center of mass of the cloud (normalized by the initial cloud distance from the center of the **CC85** wind). Along each of the curves, the diamonds and stars have the same meaning as in Fig. 9. The surface area of the clouds, after entrainment, follows $A_{\text{cl}} \propto V_{\text{cl}}^{2/3}$ as indicated by the **yellow** band in the upper panel. As discussed in Section 4.1.1, one gets $A_{\text{cl}} \propto d_{\text{cl}}^{3\gamma-2} \sim d_{\text{cl}}^3$; $\gamma = 5/3$, which is approximately followed by the largest clouds (**yellow** band in the lower panel) that do not grow and experience as much orthogonal expansion compared to their initial size as the smaller clouds (cf. Fig. 9). While for small clouds, relative expansion is important and $m_{\text{cl}} \propto d_{\text{cl}}^{23/12} \approx d_{\text{cl}}^2$ (cf. Fig. 10), which implies $A_{\text{cl}} \propto d_{\text{cl}}^{3(\gamma-1/2)} \sim d_{\text{cl}}^{3.5}$; $\gamma = 5/3$ as indicated by the **gray** band in the lower panel, albeit the difference in the slopes between the yellow and the gray bands is small (compare with Fig. 10 where the difference in the slopes is large).

Fig. C1, we find that clouds in a **CC85** wind in our simulations form much longer cometary tails. Although the mass formed (cf. Section 4.1.1 & Fig. 11) and the expansion of the tail of the cloud orthogonal to the wind between the simulation setups are comparable, there exists a difference in the estimate of the distance moved by the cloud and possibly in the rate of mass growth of clouds in the cooling regime.

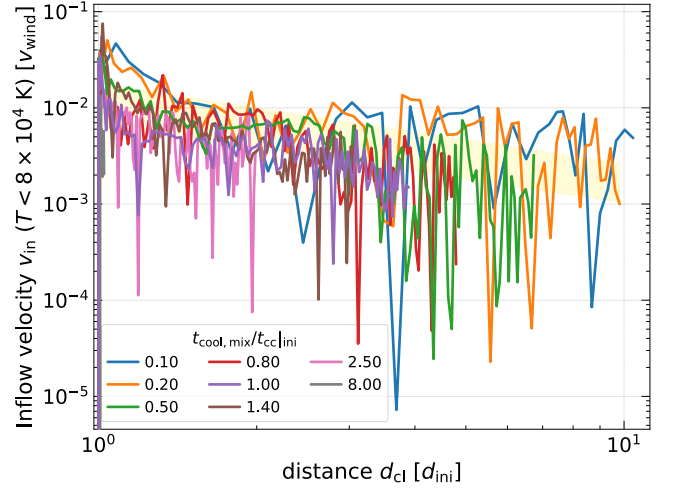


Figure B2. Evolution of the inflow velocity (in units of the wind speed at the initial cloud position) across the surface of the radiatively cooling turbulent boundary layer, identified in the same way as in Fig. B1, as a function of the distance travelled by its center of mass (normalized by its initial distance from the center of the **CC85** wind). The inflow velocity v_{in} has been calculated as the average mass-weighted velocity along the local normals used to tessellate the iso-surface of temperature at 8×10^4 K bounding the cloud. Albeit with a lot of scatter, v_{in} scales with the position of the center-of-mass d of the clouds as $v_{\text{in}} \propto d_{\text{cl}}^{-\gamma/2} \sim d_{\text{cl}}^{-5/6}$; $\gamma = 5/3$, as indicated by the yellow band.

APPENDIX D: CONVERGENCE

We demonstrate results from our convergence test on the evolution of the cold cloud mass in our simulation for the fiducial parameter, $t_{\text{cool,mix}}/t_{\text{cc}}|_{\text{ini}} = 0.2$ (cf. Table 1). For all simulations in our convergence test, a domain with an extent of about $250 R_{\text{cl}}$ in the radial direction and $22 R_{\text{cl}}$ at the initial position of the cloud in the orthogonal directions had been considered. The only exception is the simulation with the highest resolution of $R_{\text{cl}}/d_{\text{cell}}|_{\text{ini}} = 64$, where the radial extent is reduced to $100 R_{\text{cl}}$ due to computational limitations. We find that with higher resolution (increasing the value of $R_{\text{cl}}/d_{\text{cell}}|_{\text{ini}}$ at the initial position of the cloud), the cold mass in the cloud is higher at all times. However, the results across different resolutions agree within a factor of a few in the time window of our analysis. At high resolutions, the evolution of the cold mass tends to converge, although the clouds differ considerably in their morphology. The qualitative picture of cloud growth due to strong radiative cooling is well captured across all resolutions. The increased amount of cold mass with increasing resolution is not surprising, as we are able to capture the formation and evolution of smaller cold clumps when the resolution is higher. Dissipation in our simulations operates at the grid resolution, and there are no explicit dissipative terms. Consequently, with increased resolution, the grid is able to capture the mixing and cooling till smaller scales. This increased resolution causes an increase in mixing and cooling, resulting in a slightly higher transfer of mass and momentum from the hot to the cold phase, as seen in the position of the center of mass of the cloud in the right panel of Fig. D2. Therefore, the cloud travels faster and gets quickly entrained at higher resolution. A similar trend has also been previously found in our earlier works on cloud-crushing (cf. Fig. B1 in Kanjilal et al. 2021). However, **CC85** wind brings an additional complication by the faster travel of the cloud material – the wind condition depends strongly on the instantaneous position of the cloud (for example, $T_{\text{wind}} \sim d^{-2(\gamma-1)}$), which can lead to signif-

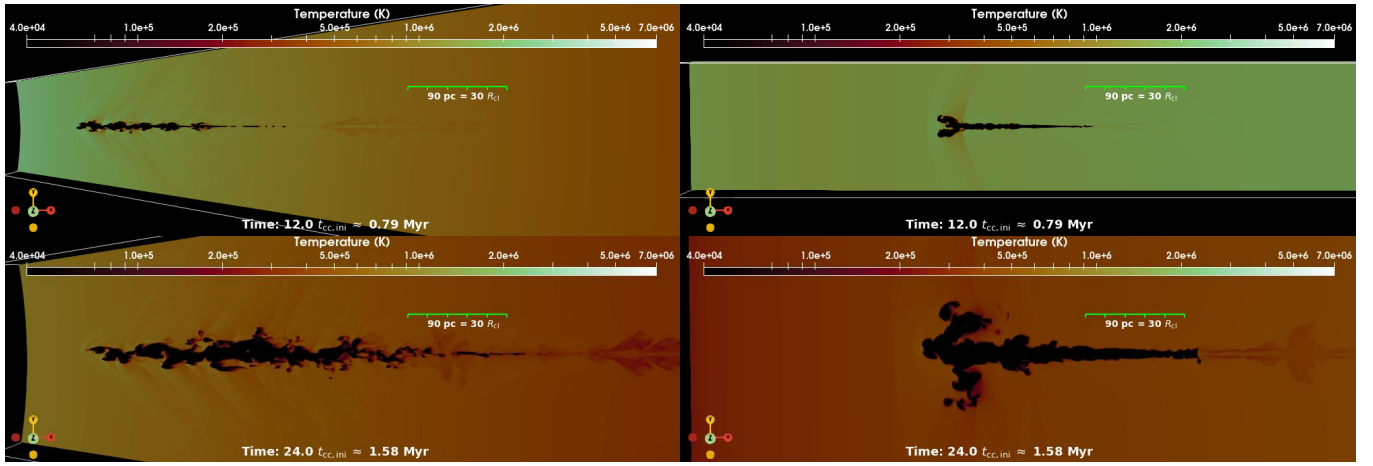


Figure C1. Slice plots of the temperature field comparing cloud-crushing simulations in a CC85 wind from our simulation (left panel) with the anisotropically expanding box model from Gronke & Oh 2020 (right panel) re-simulated here using PLUTO MHD code (Mignone et al. 2007). The anisotropically expanding box approximates the cloud dynamics in a CC85 wind using a uniform expansion of the entire simulation domain in all directions orthogonal to the direction of the wind as the cloud moves downstream (no expansion in the wind direction). Although the cold gas formed are comparable (see Section 4.1.1), the cloud morphologies are significantly different between the two simulations. In our simulations, a cloud experiences spatially different wind conditions at any particular instant, in contrast to a homogeneous wind in Gronke & Oh 2020. Except for the region around the head, which is more spread out laterally in GO20 setup, the cloud forms cometary tails, which are longer in our simulations, with comparable expansion orthogonal to the wind in both simulations. Follow the [link here](#) to see a video of the full evolution.

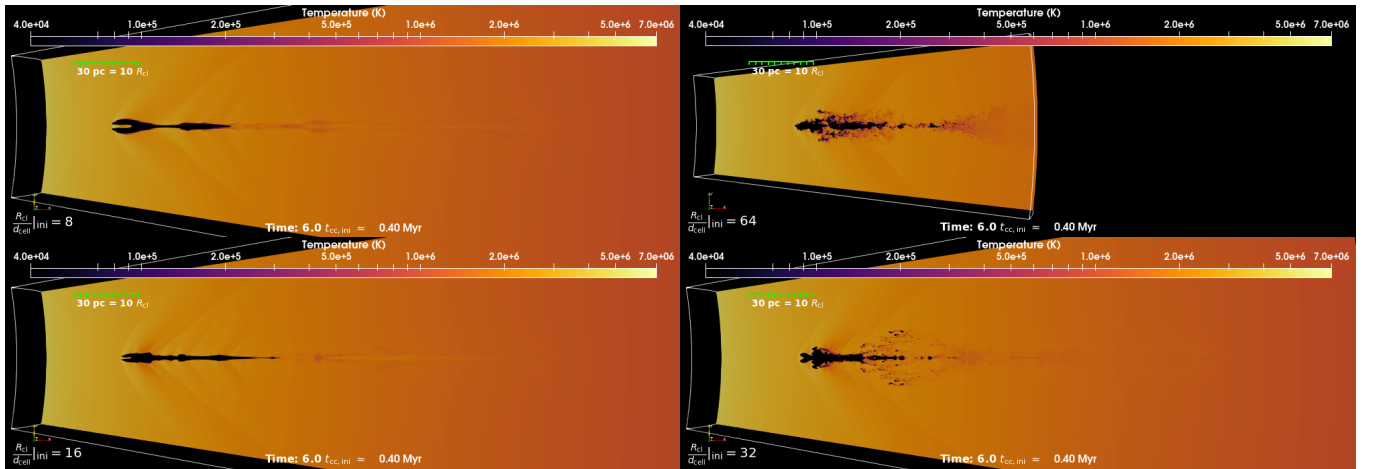


Figure D1. Slice plots of the temperature field comparing cloud-crushing simulations in a CC85 wind at four different resolutions – $R_{\text{cl}}/d_{\text{cell}}|_{\text{ini}} = (8, 16, 32, 64)$ at time $t/t_{\text{cc,ini}} = 6$. As expected, on increasing resolution, mixing at smaller scales is better resolved. For these simulations, a domain with an extent of about $250 R_{\text{cl}}$ in the radial direction and $22 R_{\text{cl}}$ at the initial position of the cloud in the orthogonal direction had been considered, with the exception of the simulation with the highest resolution of $R_{\text{cl}}/d_{\text{cell}}|_{\text{ini}} = 64$, where the radial extent of the box has been reduced to $100 R_{\text{cl}}$ due to computational limitations. Follow the [link here](#) to see a video of the full evolution.

icant differences in cloud properties across simulations at different resolutions as time progresses.

APPENDIX E: SINGLE-CLOUD MODEL FROM FB22

Fielding & Bryan 2022 (FB22 hereafter) introduced the following set of ordinary differential equations¹¹ to model how an individual cloud evolves in a hot wind.

¹¹ We ignore gravity and assume the same metallicity for both the cloud and the wind and present these equations in an equivalent but modified form.

$$\frac{d}{dt} \begin{bmatrix} d_{\text{cl}} \\ v_{\text{cl}} \\ M_{\text{cl}} \end{bmatrix} = \begin{bmatrix} v_{\text{cl}} \\ v_{\text{rel}} \left(\frac{\dot{M}_{\text{cl,grow}}}{M_{\text{cl}}} \right) + (3/8) C_{\text{drag}} v_{\text{rel}}^2 / (\chi R_{\text{cl}}) \\ \dot{M}_{\text{cl},0} (\xi^\alpha - f_{\text{mix}}/f_{\text{cool}}) \end{bmatrix}. \quad (\text{E1})$$

This provides a generic framework for the single-cloud evolution model. In this set of equations, d_{cl} is the distance travelled by a cloud, and v_{cl} and M_{cl} are its velocity and mass respectively. The relative velocity between the cloud and the wind is denoted by $v_{\text{rel}} = v_{\text{wind}} - v_{\text{cl}}$, where v_{wind} is the wind velocity. The radius of the cloud R_{cl} is a time dependent quantity and is defined as $R_{\text{cl}} = (3M_{\text{cl}}/(4\pi\chi\rho_{\text{wind}}))^{1/3}$, where ρ_{wind} and χ are wind density and the density contrast between the cloud and the background

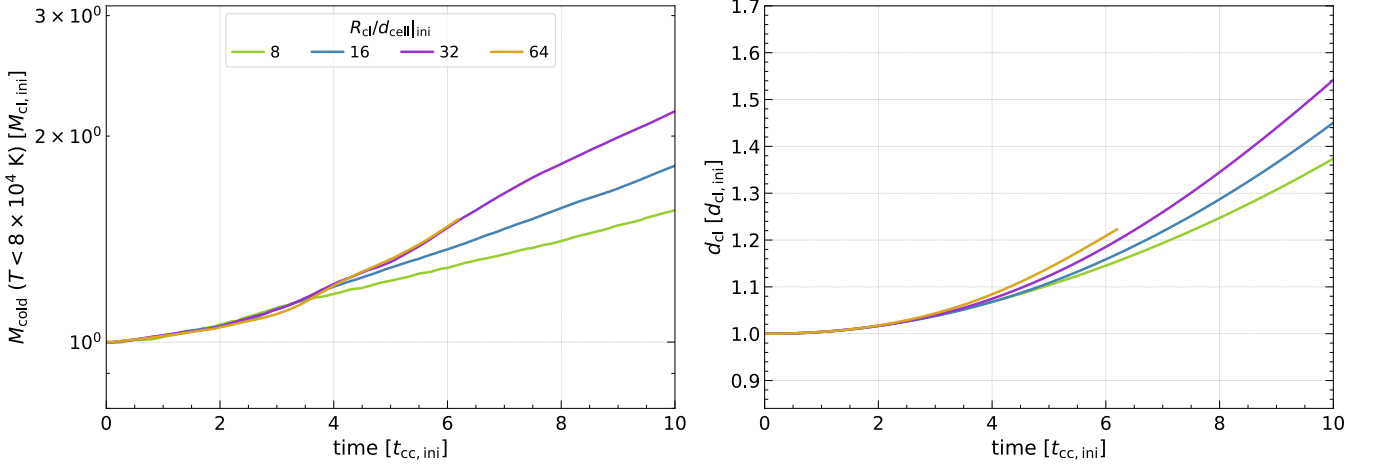


Figure D2. Comparison of the evolution of cold cloud mass (**left panel**) and distance travelled by the center of mass of the cold gas (**right panel**) in CC85 wind from our simulation at different resolutions using the fiducial parameter $t_{\text{cool,mix}}/t_{\text{cc,ini}} = 0.2$ (cf. Table 1). The resolution marked in the legend denotes the number of cells by which the cloud radius is resolved at the initial location of the cloud; a higher value corresponds to a higher resolution. The highest resolution curve with $R_{\text{cl}}/d_{\text{cell}}|_{\text{ini}} = 64$ has not been considered beyond $6 t_{\text{cc,ini}}$ as a significant amount of cold gas leaves the computational domain due to a smaller domain size compared to the simulations at lower resolutions. The highest resolution curve $R_{\text{cl}}/d_{\text{cell}}|_{\text{ini}} = 64$ is confined within the $R_{\text{cl}}/d_{\text{cell}}|_{\text{ini}} = 16$ and $R_{\text{cl}}/d_{\text{cell}}|_{\text{ini}} = 32$ curves, indicating that the cold mass growth is converged. The mass estimated at different resolutions agree with one another within a factor of a few, and their difference diminishes as the simulation resolution increases (compare, for example, the difference between the $R_{\text{cl}}/d_{\text{cell}}|_{\text{ini}} = 32$ and $R_{\text{cl}}/d_{\text{cell}}|_{\text{ini}} = 64$) indicating convergence in cloud mass. Increased mixing at high resolution causes increased momentum transfer from the hot to the cold phase causing the cloud to move faster in the wind at higher resolution.

wind, respectively. $\dot{M}_{\text{cl, grow}}$ is the rate at which cloud mass grows due to radiative cooling and is defined as $\dot{M}_{\text{cl, grow}} = \dot{M}_{\text{cl,0}} \xi^\alpha$, where $\dot{M}_{\text{cl,0}} = 3 f_{\text{turb}} f_{\text{cool}} M_{\text{cl}} |v_{\text{rel}}| / (\sqrt{\chi} R_{\text{cl}})$, as prescribed in FB22. C_{drag} is the drag coefficient due to the relative velocity between the cloud and the wind. This relative velocity also generates turbulent instabilities (like Kelvin-Helmholtz and Rayleigh-Taylor), resulting in the development of turbulent velocity with f_{turb} being the proportionality constant (similar notation was previously used by Mandelker et al. 2019, 2020, such that the mass loss rate from the cloud to the wind $\dot{M}_{\text{cl, loss}} = 3 f_{\text{mix}} f_{\text{turb}} M_{\text{cl}} |v_{\text{rel}}| / (\sqrt{\chi} R_{\text{cl}})$. The area available for cooling $A_{\text{cool}} \propto R_{\text{cl}} v_{\text{rel}} t_{\text{cc}}$ increases as the cloud stretches and mixes in the wind and forms a wake in its path defined as $A_{\text{cool}} = f_{\text{cool}} 4\pi R_{\text{cl}}^2 \sqrt{\chi}$, where the cloud-crushing time $t_{\text{cc}} = \sqrt{\chi} R_{\text{cl}} / |v_{\text{rel}}|$ is the characteristic timescale for the growth of hydrodynamic instabilities that mix a cloud. Here $\xi = R_{\text{cl}} / (f_{\text{turb}} |v_{\text{rel}}| t_{\text{cool}})$, where we consider t_{cool} as the isobaric cooling time of the mixed gas, which is assumed to be at the temperature of $\sqrt{\chi}$ times the cloud temperature T_{cl} .¹² This factor ξ bears similarity to the Damköhler number from turbulent combustion literature, introduced in the context of cloud-crushing by Tan et al. 2021. Therefore, the clouds where radiative cooling is dominant correspond to large values of ξ (i.e., small t_{cool} or large R_{cl}).

This paper has been typeset from a $\text{\TeX}/\text{\LaTeX}$ file prepared by the author.

¹² $t_{\text{cool}} = \gamma / (\gamma - 1) \left(p_{\text{wind}} / ((\sqrt{\chi} \rho_{\text{wind}} X_H / m_p)^2 \Lambda[\sqrt{\chi} T_{\text{cl}}]) \right)$, where p_{wind} is the pressure in the wind (as well as the cloud), X_H is the hydrogen density fraction, m_p is proton mass, Λ is the radiative cooling function, and γ is the adiabatic index.